Hierarchical parcel-swapping representation of turbulent mixing. Part 4. Extension to the viscous range and to mixing of scalars with nonunity Schmidt numbers

Masoomeh Behrang[1], **Tommy Starick**[2], **Isaac Wheeler**[1], **Heiko Schmidt**[2], **Alan R. Kerstein**[3], **and David. O. Lignell**[1]†

[1]350 CB, Brigham Young University, Provo, UT 84602, USA

[2]Brandenburg University of Technology Cottbus-Senftenberg, Germany

[3]Consultant, 72 Lomitas Road, Danville, CA 94526, USA

Hierarchical Parcel Swapping (HiPS) is a multiscale stochastic model of turbulent mixing based on a binary tree. Length scales decrease geometrically with increasing tree level, and corresponding time scales follow inertial range scaling. Turbulent eddies are represented by swapping subtrees. Lowest-level swaps change fluid parcel pairings, with new pairings instantly mixed. This formulation, suitable for unity Schmidt number Sc, is extended to nonunity Sc. For high Sc, the tree is extended to the Batchelor level, assigning the same time scale (governing the rate of swap occurrences) to the added levels as the time scale at the base of the $Sc = 1$ tree. For low Sc, a swap at the Obukhov-Corrsin level mixes all constituent parcels within corresponding subtrees. Well-defined model analogs of turbulent diffusivity and mean scalar-variance production and dissipation rates are identified. Simulations idealizing stationary homogeneous turbulence with an imposed mean scalar gradient reproduce various statistical properties of viscous-range and inertial-range pair dispersion and of the scalar power spectrum in the inertial-advective, inertial-diffusive, and viscous-advective regimes. The viscous-range probability density functions of pair separation and scalar dissipation agree with applicable theory, including the stretched-exponential tail shape associated with viscous-range scalar intermittency. Previous observation of that tail shape for $Sc = 1$, heretofore not modeled or explained, is reproduced. Comparisons to direct-numerical-simulation allow evaluation of empirical coefficients, facilitating quantitative applications. Parcel-pair mixing is a common mixing treatment, e.g., in subgrid closures for coarse-grained flow simulation, so HiPS can improve model physics simply by smarter (yet nearly cost-free) selection of pairs to be mixed.

1. Introduction

Turbulent mixing processes are critically important in a wide range of applications, from supernovae (Sreenivasan 2019) to phytoplankton dynamics (Kessouri

† Email address for correspondence: davidlignell@byu.edu

et al. 2018), combustion (Cabra *et al.* 2002, 2005), and pollutant dispersion (Lim *et al.* 2022). Given their ubiquitous presence, understanding and accurately modeling these processes is essential. However, this is challenging due to multiple time and length scales involved (Argyropoulos & Markatos 2015). The primary challenge in turbulent flow research is to develop models that can represent these scales effectively. Such models must capture the complexity of turbulent mixing processes with high fidelity while balancing computational efficiency, a crucial aspect for practical applications.

Hierarchical parcel swapping (HiPS) (Kerstein 2013, 2014, 2021) is a minimal model of turbulent mixing. It involves a binary tree structure in which length scales at successive tree levels decrease geometrically downward from the apex of the tree, and as originally formulated, the corresponding time scales follow inertial-range scaling. Physical fluid parcels reside at the base of the tree, such that the tree structure serves only to conveniently prescribe the time advancement of the system state, involving advection and mixing sub-processes.

Turbulent advection is modeled by introducing randomly sampled eddy events, each of which swaps the positions of two equal-size subtrees. Each parcel has the same composition as its nearest neighbor, where there is only one nearest neighbor in the binary-tree geometry. When a swap causes a composition difference between nearest neighbors, the two parcels are fully and instantaneously mixed so as to restore equality of parcel compositions. Only a lowest-level swap, in which each subtree is a single parcel, can rearrange parcel pairings and thus induce mixing. On this basis, the model induces stepwise scalar length-scale breakdown leading ultimately to mixing at a prescribed dissipation scale, nominally the Kolmogorov microscale, thus broadly idealizing the phenomenology of passive diffusive scalars in inertial-range turbulence.

This formulation implies equivalence of the advective (Kolmogorov) and mixing-dominated (Batchelor) microscales η and η_b respectively, corresponding to unity nominal Schmidt number $Sc = \nu/D$, where ν is the kinematic viscosity and D is the molecular diffusivity. Model extension to nonunity Sc has been proposed (Kerstein 2013) but not yet implemented. Instead, applications to date have introduced a different type of extension in which the parcel state is the velocity vector $\mathbf{v}$ rather than one or more scalars, enabling flow-field simulation rather than adoption of a prescribed flow parameterization (Kerstein 2014, 2021). The extension to nonunity Sc is implemented here within the flow-parameterization framework but can eventually be incorporated into the flow-simulation framework, as explained in section 5.

Extension to high Sc requires augmentation of the binary tree by appending levels at the bottom of the tree that represent the viscous-dissipation range. For this purpose, the added levels are all assigned the same time scale that applies to the bottom of the inertial range (nominally the Kolmogorov time scale). This corresponds to the physical picture of stepwise scalar length-scale breakdown induced by the smallest available eddies, hence the Kolmogorov eddies, which induce successive multiplicative compressions of viscous-range scalar structure until this process is balanced by molecular-diffusive smoothing at the Sc-dependent Batchelor scale. For low Sc, the Obukhov-Corrsin scale η_{oc} is analogous to η_b, with $\eta_{oc} > \eta$, and accordingly, homogenization across subtrees corresponding to scale η_{oc} is enforced, albeit on the basis of Bernoulli trials rather than assured homogenization.

Application of swaps to marked fluid parcels, involving no scalar content

or mixing thereof, is sufficient to time advance parcel-pair separations. The simplicity of this process allows analytical treatment and consequent deterministic advancement of the probability density function (PDF) of pair separation, complementing information gleaned from Monte-Carlo simulation. For both the inertial and dissipative regimes, it is shown that the results largely conform to known and theoretically predicted phenomenology.

Mixing phenomenology is investigated in a configuration that idealizes an imposed mean scalar gradient in statistically stationary homogeneous turbulence. Turbulent diffusivity and mean scalar-variance production and dissipation are shown to have precise mathematical meanings that allow them to be quantified straightforwardly in nondimensional form. HiPS simulations produce PDFs of scalar dissipation whose tail shapes conform to predictions of asymptotic analysis. Scalar power spectra are consistent with known scaling exponents governing the inertial-advective, inertial-diffusive, and viscous-advective ranges. Conversion factors relating HiPS analogs of Sc, η, η_b, the Obukhov-Corrsin constant β, and Reynolds number Re to their physical counterparts are evaluated by comparing HiPS and direct-numerical-simulation (DNS) results. These conversion factors enable quantitative application of HiPS to turbulent mixing processes of interest. In this context, prospects for mixing/reaction closure of under-resolved three-dimensional turbulent flow simulations are discussed.

2. HiPS model

2.1. *Model representation of flow advancement*

HiPS is based on a binary tree structure. Each level of the tree is defined by a set of nodes. Each node branches into two sub-nodes, continuing to the bottom of the tree where fluid parcels reside. All fluid properties are defined only in the fluid parcels at the bottom of the tree, though mixing length and time scales are stored at the other node levels. In contrast to other hierarchical models, there are no filtered parcel states at higher levels.

Figure 1 illustrates the basic tree structure. The tree shown has $N = 5$ levels, where N is the total number of tree levels. Nodes are indicated by circles, and fluid parcels by squares. At the bottom of the tree, fluid parcels are paired as defined by their connecting node at the previous level. Parcel proximity is defined as the level index of the nearest node connecting two parcels. In figure 1, parcel pairs (a, b), (a, d), (a, f), and (a, p) have proximities at node levels 3, 2, 1, and 0, respectively. The proximity between a and either c or d is the same (at level 2), the proximity between a and any of e through h is the same (at level 1), and the proximity between a and any of i through p is the same (at level 0). Furthermore, the ordering of parcels with the same proximity is not relevant. For example, the tree state in figure 1 is unchanged if the first four parcels a, b, c, d were written as d, c, a, b, since the parcel proximities on the tree are the same.

Turbulent stirring is modeled by rearranging parcels. This involves a sequence of *eddy events*, each of which is implemented as follows:

(i) A given node of the tree is selected within accessible levels indexed $i = 0$ to $i = N - 3$; this is the base node.

(ii) A random node (or fluid parcel if $i = N - 3$) two levels down along the left branch emanating from the base node is randomly selected, and another node (or
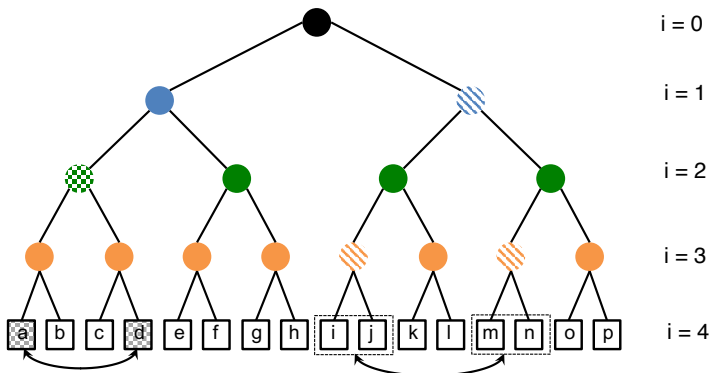
Figure 1: Schematic illustration of the binary HiPS tree showing nodes (circles) and fluid parcels (squares).

fluid parcel) is randomly selected two levels down along the right branch. These are grandchild nodes or parcels.

(iii) The two selected grandchildren of the base node are swapped (along with their subtrees in the case of swapping nodes).

Note that in step 2, grandchild nodes/parcels are selected two levels below the base node rather than selecting child nodes/parcels one level below the base node because the latter does not cause any change. The parcel proximity is what matters, not the left-to-right ordering suggested in figure 1.

Two swaps are shown in figure 1. The first is with the green checked base node at level 2. The two gray checked fluid parcels labeled a and d are randomly selected. These two fluid parcels would then be swapped. This would change the pairing of parcels: $(a, b) \rightarrow (d, b)$ and $(c, d) \rightarrow (c, a)$. The second swap selects the blue striped base node at level 1. The two orange-striped grandchild nodes are randomly selected, and the two subtrees emanating from these nodes are swapped. In this case, those subtrees consist of fluid parcels i and j being swapped with parcels m and n. Note that in the second case, parcel pairings are not changed, whereas the parcel pairings are changed in the first case. That is, parcel pairings are only directly affected when swaps happen at the base node level indexed $i = N - 3$. Pairing of previously unpaired parcels is deemed to induce micromixing (implemented as explained in section 2.4), while mixing at other levels is macromixing that affects the spatial distribution of parcel states but not the internal compositions of individual fluid parcels. The macromixing at upper tree levels $i < N - 3$ effectively *sweeps* the finer scales at lower levels while inducing a stepwise breakdown of flow structure at the scale of the eddy event (base-node level), consistent with the behavior of inertial-range turbulent eddies in real flows.

2.2. *Tree length and time scales*

As noted above, each tree level is associated with a length scale, L, and a corresponding time scale, τ, with the largest scales at the top of the tree (lowest level index in figure 1), L_0 and τ_0. The length scale at each level is a factor A of the length scale at the previous level, $L_{i+1} = L_i A$, which gives

$$L_i = L_0 A^i, \tag{2.1}$$

with $A < 1$. If we consider parcels to occupy fluid volume, then, for a binary tree, each subtree occupies half the volume as the tree above, with a length scale ratio of A. If $A = 1/2^{1/3}$, then the cube of the length scale reduction matches the putative volume reduction. This value of A corresponds to a tree representing a three-dimensional domain. In general, $A = 2^{-1/d}$ for d dimensions. In Kerstein (2013) and its sequels, $d = 1$, corresponding to $A = 1/2$, was chosen largely because the interpretation of the HiPS domain as line of sight through a planar-symmetric flow was suitable for applications of interest. This provides a larger length scale reduction for a given number of levels and parcels than for larger values of A. For reasons explained in section 3.3.2 and Appendix A, $A = 1/2$ is the default choice but the choice of another A value is shown to be advantageous in some situations.

While the domain length scale is L_0, corresponding to the sum of the length scales of all parcels, the largest eddy event at level $i = 0$ swaps half the parcels on the domain (that is half the parcels in each of the two half-trees). This corresponds to a largest eddy size $L_1 = L_0 A$, which is interpreted as the integral scale L_I. We define two additional scales. The first, l^* at level index i^* (with time scale τ^*), corresponds to a scalar with unity Schmidt number Sc. This scale marks the transition between the inertial-advective regime, and the viscous-advective regime. The other scale is denoted l_s^* at level i_s^* (with time scale τ_s^*), and is the smallest length scale for a scalar with arbitrary Sc. Section 2.5 gives further discussion. The smallest eddy length scale on the tree has a level index of $N - 3$.

We define the HiPS Reynolds number as

$$Re = \left(\frac{L_0}{l^*}\right)^{4/3} = A^{-\frac{4}{3}i^*}. \tag{2.2}$$

The time scale at each level is specified based on the turbulent inertial sub-range where the kinetic energy dissipation rate is constant (Kolmogorov's second similarity hypothesis (Pope 2000)),

$$\epsilon \sim \frac{u^2}{\tau} \sim \frac{L^2}{\tau^3}, \tag{2.3}$$

where ϵ is turbulent kinetic energy dissipation. For constant ϵ, we have $\tau \sim L^{2/3}$, which gives

$$\tau_i = \tau_0 \left(\frac{L_i}{L_0}\right)^{2/3} = \tau_0 A^{2i/3}, \tag{2.4}$$

where $L_i = L_0 A^i$ is used. Table 1 illustrates the length and time scales associated with the tree levels for $A = 1/2$.

Level	Length scale	Time scale
0	L_0	τ_0
1	$L_0/2$	$\tau_0/2^{2/3}$
2	$L_0/4$	$\tau_0/4^{2/3}$
$\vdots$	$\vdots$	$\vdots$
i	$L_0/2^i$	$\tau_0/(2^i)^{2/3}$
$\vdots$	$\vdots$	$\vdots$
N-3	$L_0/2^{N-3}$	$\tau_0/(2^{N-3})^{2/3}$

Table 1: HiPS tree length scales and time scales.

2.3. *Eddy selection*

2.3.1. *Sampling of event times*

Given the time scale, τ_i at each HiPS tree level i, eddy events are performed as follows. An eddy rate λ_i is associated with each level. We expect (on average) one eddy in time τ_i at each node of a given level, so the rate at each node is $1/\tau_i$, and the rate at all nodes of level i is

$$\lambda_i = \frac{2^i}{\tau_i}. \tag{2.5}$$

The total rate of all eddies Λ is the sum of the rates on each level. Eddy event times are then sampled from an exponential distribution corresponding to a Poisson process with mean rate Λ,

$$p(\Delta t) = \Lambda e^{-\Lambda \Delta t}. \tag{2.6}$$

Here, $p(\Delta t)$ is the PDF of spacing Δt between eddy events. The cumulative distribution function (CDF) is

$$P(\Delta t) = \int_0^{\Delta t} p(\Delta t') d\Delta t' = 1 - e^{\Lambda \Delta t}. \tag{2.7}$$

Eddy occurrence times are sampled from this CDF as

$$\Delta t = -\frac{\ln(P_r)}{\Lambda}, \tag{2.8}$$

where $P_r \in [0, 1]$ is a uniform random variate. This sampling is illustrated in figure 2.

2.3.2. *Eddy level selection*

The selection of the tree level of a sampled eddy event is described. The formulation is designed to capture the full scale range of non-negligible scalar fluctuations, thus ranging from the integral scale to the smaller of l^* and l_s^*. Specializing to a single scalar field, the required scale range depends on Sc. The tree can be extended to any number of levels below the required minimum, so the assumption that it resolves some arbitrarily small $l_s^* < l^*$ encompasses all cases.

For convenience, the inertial range of scales, $l \geqslant l^*$, is here labeled I, and the viscous scale range, $l < l^*$, is here labeled V. The rate of all eddies in the
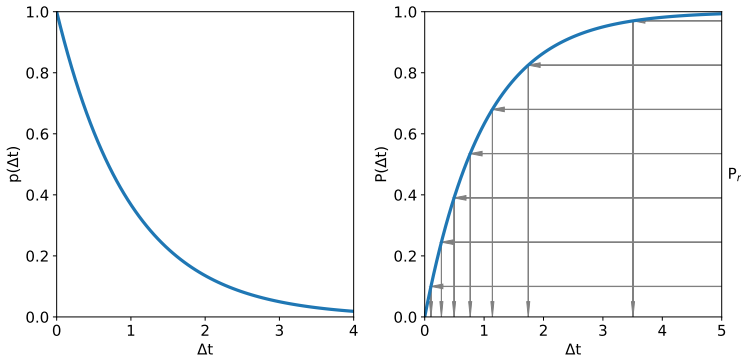
Figure 2: Illustration of sampling eddy times from $P_r(\Delta t)$.

respective ranges is denoted Λ_I or Λ_V, which are formulated below. The total rate is simply $\Lambda = \Lambda_I + \Lambda_V$. To determine the region, a uniform random variate $P_r \in [0,1]$ is selected; if $P_r \leqslant \Lambda_I/\Lambda$, region I is selected, otherwise region V is selected. We then select a particular level in the chosen region.

In the inertial range, the probability of an eddy event at level i is

$$p(i) = \frac{\lambda_i}{\Lambda_I}, \tag{2.9}$$

where $\Lambda_I = \sum_{i=0}^{i^*} \lambda_i$. Equations 2.4 and 2.5 give

$$\lambda_i = \frac{2^i}{\tau_0 A^{2i/3}}, \tag{2.10}$$

and consequently,

$$\Lambda_I = \frac{1 - (2A^{-2/3})^{i^*+1}}{\tau_0(1 - 2A^{-2/3})}. \tag{2.11}$$

This provides the CDF as

$$P(i) = \sum_{j=0}^{i} \frac{\lambda_j}{\Lambda_I} = \frac{1 - (2A^{-2/3})^{i+1}}{1 - (2A^{-2/3})^{i^*+1}}. \tag{2.12}$$

Finally, i can be sampled as

$$i = \left\lceil \frac{\log_2(1 - P_r(1 - (2A^{-2/3})^{i^*+1}))}{1 - \frac{2}{3}\log_2 A} - 1 \right\rceil, \tag{2.13}$$

where P_r is a uniform random variate on [0,1], (different from that used to select between regions I or V).

In the viscous range, the formulation for sampling eddy levels is somewhat different. In turbulent flow, the smallest eddies are nominally size η, (the Kolmogorov scale), but the associated straining and scale compression affects structures at smaller scales. Any incipient smaller-scale flow structure is dissipated by viscosity, but for $\eta_b < \eta$, where η_b is the Batchelor scale, scalar-field structure is created by scale-η eddies and down-scaled by them until its eventual dissipation

at scale η_b. HiPS scale resolution is extended down to scale l_s^* (or optionally, lower) in order to capture this scalar structure.

In HiPS, size-l^* eddy events cannot create sequentially smaller-scale structures down to arbitrarily small scales. In effect, the size-l^* HiPS eddy captures only one level of down-scaling even when applied multiple times. The full physical effect of size-l^* eddy events is nevertheless captured by implementing eddy events at all scales below l^* that are resolved by the HiPS tree, where the sampling of these events at any given scale less than l^*, and location (node) at that scale, is based on the time scale $\tau^* = \tau_0 A^{2i^*/3}$. The resulting viscous-advective scalar cascade is thus captured, as will be shown. Then at scales below l^*, the total rate of all eddies at some level i is given by $\lambda_i = 2^i/\tau^*$.

The probability of an eddy event at level i in the viscous range is then

$$p(i) = \frac{\lambda_i}{\Lambda_V}, \tag{2.14}$$

where Λ_V is

$$\Lambda_V = \sum_{i=i^*+1}^{N-3} \lambda_i = \frac{1}{\tau^*}(2^{N-2} - 2^{i^*+1}). \tag{2.15}$$

The CDF is

$$P(i) = \frac{2^{i+1} - 2^{i^*+1}}{2^{N-2} - 2^{i^*+1}}, \tag{2.16}$$

from which i can be sampled, using a uniform random variate $P_r \in [0,1]$, as

$$i = \left\lceil \log_2\left(P_r(2^{N-2} - 2^{i^*+1}) + 2^{i^*+1}\right) - 1 \right\rceil. \tag{2.17}$$

2.4. Micromixing

Micromixing can be implemented either as an instantaneous event triggered by an eddy event or continuously in time. The former is employed here owing to its simplicity and efficiency.

We assume here that scale l_s^* coincides with a HiPS level i_s^*; the general case of arbitrary l_s^* is treated in section 2.5.2. l_s^* is the scale at which molecular diffusivity (or the HiPS analog of it) balances eddy diffusivity. This corresponds physically to diffusive spreading of the scalar throughout a level i_s^* subtree over the time period corresponding to the mean time between eddy events at a given level i_s^* base node. For all model case studies and analyis presented here, this balance is approximated using the following idealized treatment. Immediately after an eddy at a level i_s^* base node is implemented, parcels in each of the two subtrees emanating from the base node are instantaneously mixed to the mean scalar value of the parcels in the given subtree. The scalar then has a uniform value in each of the two subtrees (but the value is generally different in the two subtrees). A repetition of the same eddy and subsequent mixing can then impose uniformity across the two subtrees, but nonuniformity can be reintroduced by a subsequent level-$(i_s^* - 1)$ eddy that removes and replaces one of the two subtrees below the base node.

If $i_s^* = N - 3$, then each subtree is a parcel pair, corresponding to the mixing protocol in Kerstein (2014). For two parcels a and b, the mixing process for the

scalar ϕ specializes to

$$\phi_{mix} = \frac{\phi_a + \phi_b}{2}. \tag{2.18}$$

For future applications, other micromixing formulations might be advantageous. For example, mixing using a weighting function may be desired. For variable-density mixing such as in combustion, a mass-weighted mixing rule could be applied. A further refinement, specialized here to $i_s^* = N - 3$ for illustration, is to evolve each scalar ϕ in two parcels a and b of a pair continuously in time, governed by the differential equations

$$\begin{aligned}
\frac{d\phi_a}{dt} &= \frac{\phi_b - \phi_a}{\tau}, \\
\frac{d\phi_b}{dt} &= \frac{\phi_a - \phi_b}{\tau},
\end{aligned} \tag{2.19}$$

where τ is nominally τ_s^*, possibly with an order-unity constant factor applied. These equations have an analytic solution that is convenient for application.

2.5. *Sc dependence*

In section 2.2, we defined l^* as the transition between the inertial-advective and viscous-advective regimes, and is the smallest length scale for a unity Sc scalar. It is analogous to the Kolmogorov scale η, and the two scales are proportional, (see section 4). Similarly, l_s^* is the smallest length scale for a scalar of arbitrary Sc. It is analogous to the Batchelor scale η_b (for $Sc > 1$), or the Obukhov-Corrsin scale η_{oc} (for $Sc < 1$), and is proportional to η_b or η_{oc}, as appropriate.

We define the HiPS Schmidt number as

$$Sc = (l^*/l_s^*)^{p_s}. \tag{2.20}$$

For $Sc \geqslant 1$, we have $p_s = 2$. This follows by analogy to a physical flow, for which $\tau_{\eta_b} = \tau_\eta$ in the viscous-advective regime, with $Sc = \nu/D$, $\nu = \eta^2/\tau_\eta$, and $D = \eta_b^2/\tau_{\eta_b}$. For $Sc \leqslant 1$, $p_s = 4/3$. Again, by analogy to a physical flow, this follows from the same relations as above, but $D = \eta_{oc}^2/\tau_{\eta_{oc}}$, and instead of $\tau_\eta = \tau_{\eta_b}$, we have $\tau_{\eta_{oc}} = \tau_\eta(\eta_{oc}/\eta)^{2/3}$ in the inertial range (using equation 2.4).

We now relate the Sc and associated scales to the HiPS tree.

2.5.1. *Discretized Sc values*

For clarity, the restriction of l_s^* values to HiPS levels is initially maintained, followed in section 2.5.2 by generalization to arbitrary l_s^*. In general, a HiPS simulation may be performed with an arbitrary number of scalars with different Sc. Figure 3 shows schematics of two scalars on a given tree. The horizontal lines correspond to tree levels, with the decreasing line width from top to bottom corresponding to the decreasing length scale with increasing level index. Two scalars are shown with $Sc < 1$, and $Sc > 1$. The level i^* is at the same location in both schematics since a single HiPS flow is considered. Each scalar is mixed across the respective left and right subtrees emanating from nodes at level i_s^*, as indicated. For the $Sc > 1$ scalar pictured, these left and right subtrees are simply parcel pairs.

The Sc is related to the tree levels i^* and i_s^* as follows. Sc was defined in equation 2.20 as $Sc = (l^*/l_s^*)^{p_s}$. Equation 2.1 gave $L_i = L_0 A^i$, and we have
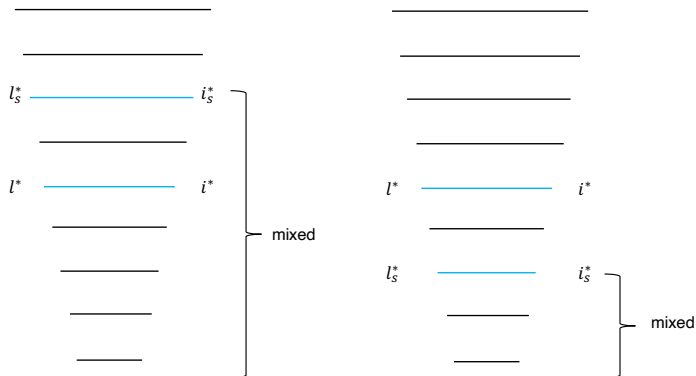
Figure 3: Schematic of the HiPS tree levels for low (left) and high (right) Sc scalars for Sc corresponding to tree levels.

$l^* = L_{i^*}$ and $l_s^* = L_{i_s^*}$. These give

$$Sc = A^{p_s(i^* - i_s^*)} = A^{-p_s \Delta i}. \qquad (2.21)$$

For $A = 1/2$, and $p_s = 4/3$ for $Sc \leqslant 1$, we have $Sc = 4^{2\Delta i/3}$ giving $Sc \approx 1$, 0.4, 0.16, 0.062, 0.025, for $\Delta i = 0$, -1, -2, -3, -4, respectively. For $Sc \geqslant 1$, $p_s = 2$, and $Sc = 4^{\Delta i} = 1$, 4, 16, 64, 256, for $\Delta i = 0$, 1, 2, 3, 4, respectively.

2.5.2. *Arbitrary Sc*

The formulation presented above identifies Sc values associated with integer levels of the HiPS tree. Arbitrary Sc corresponds to scalars with l_s^* between two HiPS tree levels, and i_s^* may not be an integer. For a scalar with a given Sc, i_s^* is computed as $i_s^* = i^* - (\log Sc)/(p_s \log A)$, or

$$Sc < 1: \qquad i_s^* = i^* - \frac{3 \log Sc}{4 \log A}, \qquad (2.22)$$

$$Sc > 1: \qquad i_s^* = i^* - \frac{\log Sc}{2 \log A}. \qquad (2.23)$$

Levels i_- and i_+ are considered for the lower and upper levels bounding i_s^*. Refer to figure 4 for a schematic. Eddy events that occur on levels at or above i_+ result in mixing of the scalar across each of the left and right subtrees emanating from the level i_+ eddy node. For a level i_- eddy event, the scalar is mixed across the two subtrees of the level i_- node with probability p_-, where

$$p_- = \frac{i_+ - i_s^*}{i_+ - i_-} = i_+ - i_s^*. \qquad (2.24)$$

The second equality holds since $i_+ - i_-$ is always unity. This probability is linear in index space and takes a value of 1 when $i_s^* = i_-$ and a value of 0 when $i_s^* = i_+$. Using equations 2.1, 2.4, and 2.5, p_- can be written as

$$p_- = \frac{\log(l_s^*/l_+)}{\log(l_-/l_+)} = \frac{\log(\lambda_s^*/\lambda_+)}{\log(\lambda_-/\lambda_+)}. \qquad (2.25)$$

This form illustrates that while there is a linear interpolation of p_- in index space, the corresponding interpolation between eddy lengths, times, or rates is
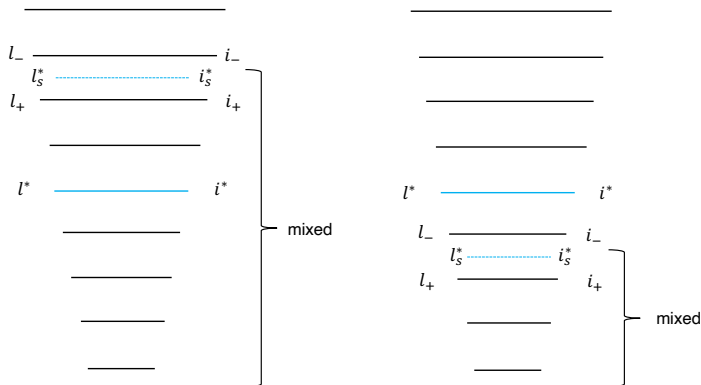
Figure 4: Schematic of the HiPS tree levels for (a) low Sc and (b) high Sc scalars.

logarithmic, consistent with the geometric progression of the scales with tree level.

3. Results

3.1. Simulated mixing configuration

As formulated in the previous sections, HiPS simulations correspond to scalar mixing in homogeneous turbulence. In the following, the scalar is evolved subject to a mean gradient, which is imposed using a jump-periodic boundary condition. This results in a statistically stationary scalar field for comparison with DNS. The scalar field is initialized to be uniform in each half of the tree, with a difference in value of $\Delta\phi_0$. The scalar gradient is then $\nabla\langle\phi\rangle = \Delta\phi_0/(L_0/2)$, giving a dimensionless scalar gradient of $G = 2$, when $\Delta\phi_0$ is taken as the reference scalar value and L_0 is the reference length scale.

For discussion of the jump-periodic condition, consider a hypothetical domain with $L \gg L_0$ and containing a size L_0 HiPS domain. The largest eddies at level-0 swap quarter-trees corresponding to half the HiPS fluid volume. Half of these eddies would involve transport across the domain center of a size-L_0 domain, and half would involve transport between size-L_0 domains. The scalar in a half-tree changes by $2\Delta\phi_0$ from one domain to the next. The jump-periodic condition is then implemented so that in half of the level-0 eddy events, the quarter-tree that is swapped from right to left has its scalar values decreased by $2\Delta\phi_0$, while the values are increased by $2\Delta\phi_0$ in the other quarter-tree that moves from left to right. This formulation results in the scalar gradient being present only at the integral scale of the tree. Subtrees of any given half-tree have mean values equal to that of their parent half-tree.

3.2. Representative instantaneous scalar profiles

To evaluate the HiPS model, three turbulence properties are studied: scalar spectra, dispersion, and scalar dissipation rate. First, we show basic simulation results of scalar mixing to highlight the qualitative behavior of the mixing model. Figure 5a shows a scalar profile plotted against parcel index for $Sc = 1$. Ten levels are used. In this simulation, the parcels are initialized as described in the previous section, but the jump-periodic boundary is not enforced, which results in decay of
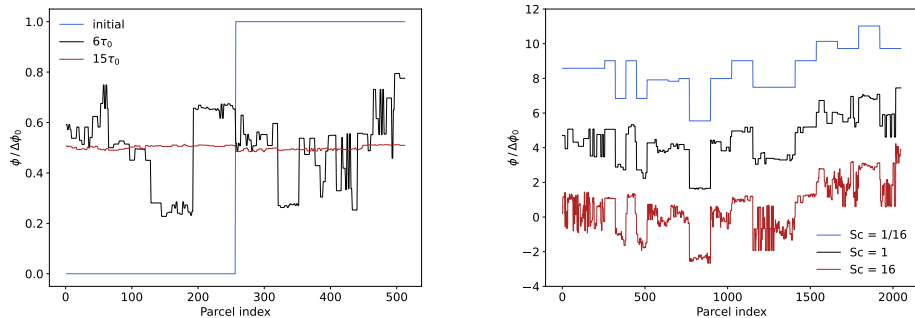
Figure 5: Passive scalar versus parcel index (a) at three times in unsteady flow; and (b) for three Schmidt numbers in the steady flow, with profiles shifted vertically by 4 and 8 units for clarity.

the parcels towards their global average. The plot shows initial, intermediate, and nearly-mixed profiles at $0\tau_0$, $6\tau_0$, and $15\tau_0$. Multiple realizations can be computed to gather statistics and compute quantities such as joint scalar PDFs.

For a tree with $N = 10$ and $Sc = 1$, we have $i^* = 7$ and $Re = A^{-4i^*/3} \approx 645$. Simulations with the same Re, but higher Sc, will have additional tree levels, as outlined above.

Figure 5b shows scalar profiles versus parcel index for three Schmidt numbers of 1/16, 1, and 16 with the jump-periodic condition used. For clarity, the curves for $Sc = 1$ and $Sc = 16$ have been shifted upwards by 4 and 8 units, respectively. As the Schmidt number increases, the HiPS-analog of diffusivity decreases, and fluctuations occur at smaller length scales. All three scalars were transported in the same simulation, so that the structures observed in the figure are consistent for the three scalar profiles.

3.3. HiPS dispersion

3.3.1. Background

The dispersion of a particle pair under the influence of turbulence is a fundamental problem in fluid dynamics (Elsinga *et al.* 2022). Dispersion refers here to the separation time history of an initially close pair of particles. Predictions for turbulent dispersion of particle pairs date back to 1926, when Richardson (1926) published an empirical approach indicating that the mean squared separation, $\langle Y^2 \rangle$, grows as the third power of time, t^3 in inertial-range turbulence (Jullien *et al.* 1998). Obukhov (1941) considered dispersion in terms of Kolmogorov's similarity theory. For dispersion in the inertial subrange and after an initial induction time, particle dispersion $\langle Y^2 \rangle$ is given by $\langle Y^2 \rangle = g\epsilon t^3$, where g is the Richardson constant. This dispersion scaling follows dimensionally if the dispersion in the inertial range depends only on ϵ and time t.

3.3.2. Analysis of parcel-pair dispersion

Using the approach proposed in Kerstein (2013), the dispersion properties of HiPS are analysed by deriving a differential equation for the evolution of the probability of pair separation at given tree level. In HiPS, the separation between two parcels of proximity i (defined above) is AL_i. For convenience, we refer to parcel separation level as the minimum number of levels k that need to be

traversed to get from one parcel to another along a connected path within the HiPS tree. Then in figure 1, parcels a and b have separation $k = 1$ levels, parcels a and d have separation $k = 2$ levels, and parcels a and k have separation $k = 4$ levels. Parcel separation index k is related to proximity index i as $k = N - 1 - i$, giving increasing k with increasing parcel separation. We consider separation levels $k \in \{1, 2, \ldots, N - 1\}$.

Consider an ensemble of HiPS trees with n_p total parcel pairs across all trees that initially have separation index $k = 1$. Parcel separations must initially increase, but then eddy events can either increase or decrease the pair separation. The rate of change of the number of pairs with separation index k is given by

$$\frac{dn_k}{dt} = I_{k-1}n_{k-1} + D_{k+1}n_{k+1} - (I_k + D_k)n_k. \tag{3.1}$$

Here, I and D are the rates of eddy events that cause an increase I or a decrease D in parcel pair separation. The subscripts on I and D indicate the separation *from which* the increase or decrease occurs. $I_{k-1}n_{k-1}$ is the rate of eddy events that increase the separation index from $k-1$ to k, times the number of pairs with separation index $k-1$, which gives the rate of change of the number of pairs with separation index k caused by increases from separation index $k-1$. The first two terms on the right-hand side of equation 3.1 create pairs with separation index k from neighboring index values (increase from $k - 1$ or decrease from $k + 1$). The third and fourth terms remove pairs of index k as they are increased or decreased to neighboring levels $k + 1$ and $k - 1$. Increases from $k - 1$ to k occur by separation-level-k eddy events, and $I_{k-1} = 1/\tau_k$, where τ_k is the time scale at the tree level corresponding to separation index k. Similarly, decreases from $k + 1$ to k occur by separation-level-$(k + 1)$ eddy events, and $D_{k+1} = 1/(2\tau_{k+1})$. The $1/2$ factor on D is because half of such eddy events decrease the separation and half leave it unchanged, depending on the subtrees chosen for the swaps.

If we divide equation 3.1 by n_p then we have the fraction of parcel pairs for separation index k, which we can interpret as a probability P_k of separation level k. This corresponds to a classic birth-death process, where the evolving separation of a given parcel pair is a continuous-time Markov chain (Crawford *et al.* 2018). Parcels with separation $k = 2$ correspond to the i^* level. Then $\tau_k = \tau^*(L_k/l^*)^{2/3} = \tau^* A^{\frac{2}{3}(2-k)}$. Let $B = A^{2/3}$ and $T = t/\tau^*$; reordering terms we can write equation 3.1 as

$$\frac{dP_k}{dT} = B^{k-2}P_{k-1} - \left(B^{k-1} + \frac{B^{k-2}}{2}\right)P_k + \frac{B^{k-1}}{2}P_{k+1}. \tag{3.2}$$

This is a system of coupled differential-difference equations with a tridiagonal matrix form. The initial condition is $P_1 = 1$, $P_{k>1} = 0$. The matrix of coefficients of P is singular since $\sum_k P_k = 1$, so we solve for $k = 1$ to $k = N - 2$, with $P_{N-1} = 1 - \sum_{k=1}^{N-2} P_k$. Note that for $k = 1$, the first and third additive terms in equation 3.2 are zero since there are no eddy events at the tree level corresponding to $k = 1$ ($i = N - 2$). Similarly, the second and fourth terms are zero for $k = N - 1$ since there are no levels above the apex of the tree. Equation 3.2 is solved analytically by an eigendecomposition.

Figure 6 shows results of this analysis for a tree with N=16 levels. The probabilities P_k are plotted versus level separation index k for several times on linear and log scales. As noted, the time advancement is initialized with $P_1 = 1$,

$P_{k \neq 1} = 0$. The P_k profiles then migrate to higher k in time. At large T, a stationary distribution for a bounded k range is reached, which is given by

$$P_k = \frac{2^{k-1}}{\sum_{j=1}^{N-1} 2^{j-1}} = \frac{2^{k-1}}{(2^N - 2^{N-1} - 1)}. \tag{3.3}$$

This simply reflects that a given parcel's partner in the pair can have one position that has separation index $k = 1$, two positions with separation index $k = 2$, four positions with separation index $k = 3$, etc., consistent with the geometric growth of the number of parcels with tree level. After sufficient time, the partner location is statistically independent of the given parcel's location, resulting in stationarity. The final PDF at time $t/\tau_\eta = 8000$ in figure 6b has the functional form corresponding to stationarity.

The reasoning that yields the dependence $P_k \propto 2^k$ does not depend on details such as the k dependence of the coefficients of the terms in equation 3.2 so it is of particular interest to assess the physical meaning of this result. For this purpose, the argument k is transformed into the physical-space pair-separation coordinate r based on conservation of probability expressed as $P_k \Delta k = P(r) \Delta r$ where $\Delta k \equiv 1$. The estimate $\Delta r \approx (dr/dk) \Delta k$ where $r \propto A^{-k}$ gives $\Delta r \propto r$, reflecting the geometrical progression of level separations. Combining these results,

$$P(r) \propto 2^k / r \propto r^{-1 + \ln 2 / \ln(1/A)} \tag{3.4}$$

is obtained.

The default value $A = 1/2$ then corresponds to constant $P(r)$. Stationarity requires $P(r)\,dr$ to scale as the d-dimensional volume element $r^{d-1}\,dr$, so $P(r) \propto r^{d-1}$. As implied by the counting of parcel pairs with level-k separation, equation 3.4 gives $d = 1$ for $A = 1/2$. By construction, this is consistent with the line-of-sight interpretation of HiPS for this A value.

The A value for which $d = 3$ is also of interest for the purpose of consistent comparison with three-dimensional numerical pair-dispersion results. This corresponds to $A = 2^{-1/3}$, which is 0.8 to a good approximation. In Appendix A this is shown to be an advantageous choice for an additional unrelated reason. $A = 1/2$ nevertheless retains it suitability for planar-symmetric cases and is advantageous more generally because its cost efficiency makes high-intensity turbulent flows computationally accessible. This A value is therefore adopted with the exception of a single data comparison for which $A = 0.8$ is used.

Given P_k, the mean square separation is given by

$$\langle Y^2 \rangle = \sum_{k=1}^{N-1} Y_k^2 P_k = \sum_{k=1}^{N-1} l^{*2} A^{2(3-k)} P_k. \tag{3.5}$$

Figure 6c shows the results of this analysis for a tree with N=16 levels. The mean square separation and time are normalized by l^{*2} and τ^*, respectively. The dispersion increases with the cube of time in accordance with Richardson's result, but this only becomes clear for a tree with about 14 levels. Cases with up to 100 levels show a slope of 3.0 during most of the transient dispersion regime. Note that HiPS has a restricted domain size so that for a given Reynolds number (or number of tree levels), the domain only includes one integral scale. This does not severely limit dispersion in terms of Richardson scaling since that analysis is restricted to inertial-range scales smaller than the integral scale.

A fit to the dispersion data gives $g\epsilon = 0.00751$. Using ϵ from equation 4.7 in

(a)   (b)

(c)   (d)
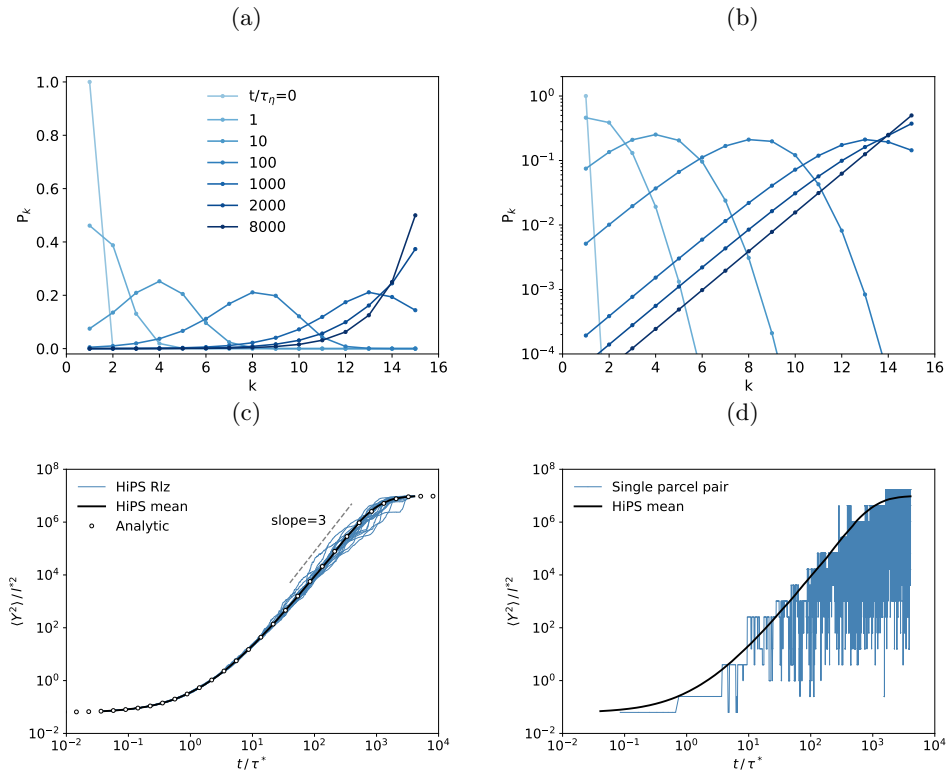
Figure 6: Probability of level separation k at several times: (a) linear and (b) log scales as solution to equation 3.2; (c) time dependence of mean square parcel-pair separation: individual HiPS realizations (abbreviated "HiPS Rlz" in the legend), the mean over 100 realizations, and the analytic equation 3.2; (d) time dependence of mean square parcel-pair separation over 100 HiPS realizations and of the square of the separation of a single representative parcel pair.

section 4, below, gives $g = 13.9$. Values of g vary widely in the literature. Sawford (2001) presents a review of turbulent dispersion and notes that "Theoretical estimates of g span nearly an order of magnitude from 0.06 to 3.52, with kinematic simulations giving the lowest values and the two-point closures generally giving the largest." DNS of dispersion give values of $g \approx 0.6$ (Sawford & Pinton 2013). The large discrepancy between HiPS and empirical g values might reflect the noted disadvantages of the choice $A = 1/2$. The possibility of a more accurate result using the preferable value $A = 0.8$ is impractical to assess owing to the prohibitive computational cost of running the scalar mixing simulations needed to determine ϵ for this A value.

3.3.3. *HiPS simulation of dispersion*

In addition to dispersion results obtained by solving equation 3.2, pair dispersion statistics from simulated HiPS realizations are shown in figure 6c. The HiPS dispersion data collection is done as follows. Parcels are indexed from left to right starting at 0, and each parcel forms a pair with its initial neighbor with separation $k = 1$. The locations of the parcels are tracked with an index array Q, where Q_i is the integer location of parcel i. Initially, $Q_i = i$. Parcels (0, 1)
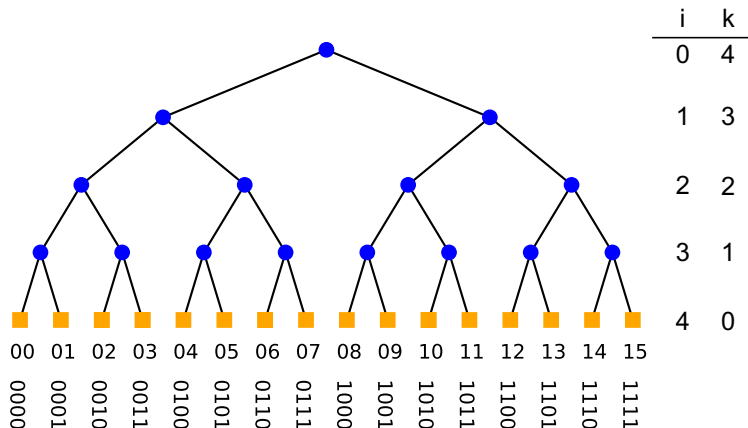
Figure 7: Simple HiPS tree, with parcel indices labeled in decimal and binary. The level index i and parcel separation level k are indicated.

form a pair, parcels (2, 3) form a pair, etc., and locations of the parcels in the pairs are (Q_0, Q_1), etc. The binary representation of these indices gives the path to the parcel location. For instance, consider parcel 03 in figure 7. For the five level tree shown, this parcel has the binary address 0011. Each digit represents a node below the root; a zero denotes the left branch and a one denotes the right branch. To get to parcel 03 we go left (0), left (0), right (1), right (1). The level separation between parcel i and its neighbor j is $k_{i,j} = \lfloor \log_2(i \oplus j) \rfloor + 1$, where $\oplus$ is the bitwise exlusive-or operator: binary digits are compared at each position and given a 0 if the digits are equal and a 1 otherwise. So $0011 \oplus 1101 = 1110$. The position from the right of the leading 1 is related to the separation index: $k_{3,13} = \lfloor \log_2(1110) \rfloor + 1 = 4$ The distance of a parcel i to its partner j is then $Y_{i,j} = l^* A^{3-k_{i,j}}$.

In figure 6c the mean square parcel pair separation is shown for a HiPS simulation with 16 levels run for $10\tau_0$. The figure shows the mean square parcel separation over 100 realizations, which gives results identical the results of the dispersion analysis in section 3.3.2. This agreement effectively serves as a verification of the HiPS numerical implementation. In addition to the mean across all realizations, several curves are shown illustrating the evolution of the mean square parcel separation in single realizations, each of which time advanced 2^{15} initial pairs of adjacent parcels. These fluctuate about the ensemble mean, and it is seen that the fluctuations increase with the magnitude of the mean square separation.

Figure 6d shows the square of the parcel separation of a single pair of parcels during a single realization, along with the mean square parcel separation over all pairs in all 100 realizations. The time history of the single pair shows the squared separation at times corresponding to every 1000th eddy event. With 16 tree levels and a simulation time of $10\tau_0$, around 50 million eddy events occur so the full resolution of the pair evolution cannot be clearly shown, but the figure gives an indication of the behavior of the representative parcel pair. The discrete nature of the HiPS tree levels is clearly evident with parcels occupying only discrete values of separation (in this case $N - 1 = 15$ separation levels). Note that the parcel pair experiences events that both increase and decrease the dispersion.

At later times, the pair is increasingly separated. This is because the number of positions at a given separation increases geometrically with the separation level, as noted above. It is seen that even at late times and high separation, the pair is still subject to episodes of very low separation. This is because HiPS advection is consistent with fluid incompressibity, which requires increases and decreases in parcel-pair separation so as to produce no overall net expansion or compression. The balance between increasing and decreasing separation depends on the effective dimensionality d. For the case shown, corresponding to $d = 1$, the episodic decreases to low separation are more frequent than they would be for larger d. This is a possible explanation of the small g value that is obtained, a point that is considered further in section 3.3.4.

3.3.4. *Analytical dispersion results extending into the viscous range*

In contrast to figure 6 that shows the dispersion PDF in the inertial range, figure 8 shows the PDF in the viscous range. The PDF was evaluated for a tree with 81 levels by solving equation 3.2 with B set to unity, reflecting the uniformity of time scales across tree levels within the viscous range. The solution for the initial condition $P_1 = 1$, $P_{k>1} = 0$ is shown as solid lines in the figure.

Appendix A presents an analysis of the PDF of parcel-pair separation that approximates equation 3.2 in the viscous range, for which $B = 1$, by Taylor expanding the terms on the right-hand side. This reduces the set of differential-difference equations to a single partial differential equation, equation A 3, reproduced here:

$$\frac{\partial P_k}{\partial T} = -V \frac{\partial P_k}{\partial k} + D \frac{\partial^2 P_k}{\partial k^2}, \tag{3.6}$$

where the two terms on the right-hand-side are drift and diffusion terms, respectively, and V and D are constants. For the specified initial condition on an unbounded domain, the solution, equation A 4, is Gaussian, corresponding to the parabolas plotted as symbols in figure 8. Owing to the Neumann condition at each end of the k range, deviations of the exact solution of equation 3.2 from the Gaussian shape are seen. The deviations could also reflect approximations in the derivation of equation 3.6, but the good agreement seen for the times and k values least affected by the boundary conditions indicates that this equation closely approximates equation 3.2.

On this basis, the log-normal PDF shape that is obtained by transforming from P_k in equation A 4 to $P(r)$, given in equation A 5, is reproduced here:

$$P(r) = \frac{1}{r(4\pi \hat{D}T)^{1/2}} \exp\left(\frac{[\ln(r/r_0) - \hat{V}T]^2}{4\hat{D}T}\right), \tag{3.7}$$

where $\hat{V} = V \ln(1/A)$ and $\hat{D} = D[\ln(1/A)]^2$, likewise closely approximates the large-k similarity solution of equation 3.2. This reproduces the log-normality of the viscous-range pair-separation PDF that has been obtained theoretically (Lundgren 1981). As explained in Appendix A, the theory predicts numerical coefficients of the log-normal distribution that govern the relative strengths of the drift and diffusion terms. Owing to the A dependence that is introduced by transforming from argument k to argument $r \propto A^{-k}$ as in the derivation of equation 3.4, the corresponding coefficients in equation 3.7 depend on A. For $A = 1/2$, the strength of the diffusion term relative to the drift term exceeds the theoretical ratio. Exact agreement with the theoretical ratio is obtained for
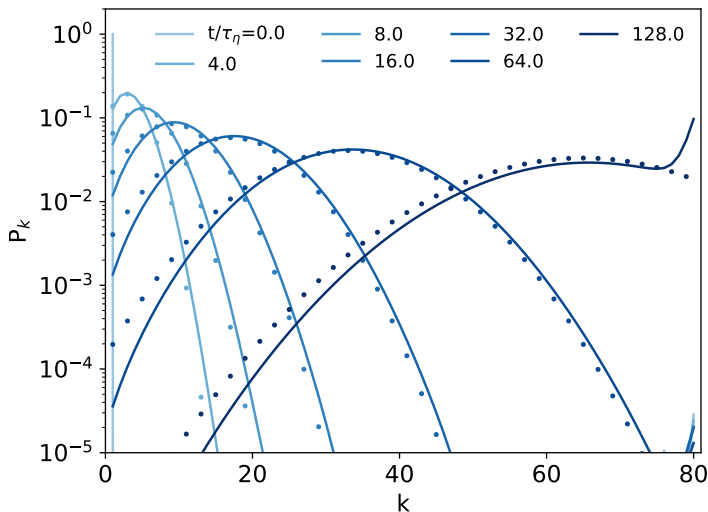
Figure 8: PDF of level separation k in the viscous regime for a tree with 81 levels. Lines are solution of equation 3.2 with $B = 1$; symbols are the analytical solution, equation A 4.

$A = \exp(-2/9)$, which is close to 0.8. This reinforces the preference for $A = 0.8$ on theoretical grounds. These observations provide context for the results that are presented next.

Figures 6 and 8 show dispersion PDFs in the inertial and viscous ranges, respectively. In figure 9, we show dispersion PDFs for a case that spans both the inertial and viscous ranges. An equation analogous to equation 3.2 is solved, but viscous-range phenomenology is introduced for k values less than a designated pair-separation level k^* corresponding to the transition between the inertial and viscous ranges. This is done by enforcing uniform time scales $\tau_k = \tau_{k^*}$ for separation levels $1 \leqslant k \leqslant k^*$.

Figure 9 shows dispersion PDFs $P(r)$, where $r = A^{1-k}$ is the pair-separation distance for any given k. Model results are compared to DNS results from Scatamacchia et al. (2012) and the sensitivity of the HiPS results to the value of A is examined. $A = 0.8$ is taken to be the base case owing to its consistency with theory.

The initial condition is constructed to be qualitatively similar to that of Scatamacchia et al. (2012) by matching a linear profile to a parabolic profile (on log scales). The peak of the DNS initial PDF is close to $r/\eta = 1$. The relationship between η and k^* is not known a-priori. In principle it could be evaluated empirically using the procedure applied in section 4, but as noted in section 3.3.2, the requisite simulations are unwieldy for $A = 0.8$. Instead, the initial profile is adjusted horizontally on the $A = 0.8$ plot so as to obtain the best qualitative agreement between model and DNS results. This implicitly specifies the relationship between η and k^*, but this is of no further interest because no other results are shown for $A = 0.8$. Then for $N = 68$ levels and $k^* = 40$, the k location of linear-to-parabolic transition of the initial PDF profile, denoted k', is set to 24. In order to isolate the A sensitivity from other adjustments, these
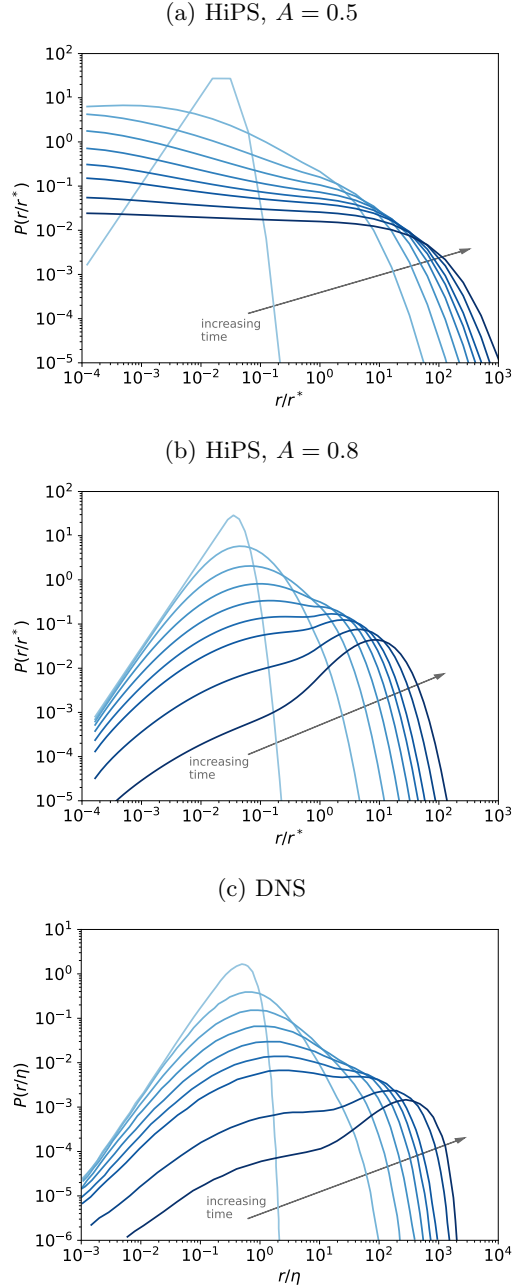
Figure 9: Dispersion PDFs: (a) HiPS, $A = 0.5$; (b) HiPS, $A = 0.8$; (c) DNS results from Scatamacchia *et al.* (2012). The times shown are at t/τ_η of 0, 10, 20, 30, 40, 50, 60, 80, and 110. Note that the initial condition corresponds to $t/\tau_\eta = 10$ in Scatamacchia *et al.* (2012) (so their times are 10 units higher). Note the different axes scales used between the model and the DNS, owing to differences between η and k^* (and corresponding r^*).

settings, in terms of the r coordinate, are also used for $A = 0.5$. Transformation back to k for this A value gives $N = 26$, $k^* = 14$, and $k' = 8$.

Another consideration is the relationship between τ_η and its model analog τ^*, which affects both event frequencies and the specification of normalized data-collection times. We have taken these time scales to be equal, which yields results that are satisfactory for present purposes.

The theory result for the relative strengths of drift and diffusion is specific to the viscous range. Nevertheless, the HiPS representations of the viscous and inertial ranges differ only in a particular detail, so the theory result implies that the choice $A = 0.8$ is likely to yield improved results relative to $A = 0.5$ even if it is not the precisely optimal choice. Comparison of the $A = 0.8$ and DNS results supports this expectation. Indeed, given that the choice of k' is the only degree of freedom that is tuned in this comparison, the results suggest that the model has considerable predictive ability.

This provides validation of the associated analysis in Appendix A, thus providing a reliable framework for interpretation of the results in figures 9b and 9c. As noted, equation 3.7 governing the viscous range corresponds to drift and diffusion in terms of $\ln r$ with constant transport coefficients. For the more general setting in which the coefficients of the terms in equation 3.2 have any prescribed k dependencies, that equation embodies the same phenomenology except that the transport coefficients are now r dependent in a manner governed by the prescribed k dependencies.

On this basis, the phenomenology underlying the time development of the PDF shapes can be viewed in terms of the combined influences of drift and diffusion. The rapid depletion at small r and the emerging shoulder suggest ongoing drift of probability out of the viscous range that encounters a bottleneck in the inertial range where time scales progressively increase. The small-r slope decreases in time rather than increasing toward the r^2 stationary solution that diffusion dominance would imply. Drift-dominated evolution is also indicated by the emergence of a large-r dome that seems to be approaching an invariant shape that slowly broadens as it drifts rightward.

Before these late-time features emerge, there is a brief transient appearance of a marginally bimodal shape. This transient is associated with bunching of the large-r PDF tails in the plot format, followed by greater separation of the successive tails as the dome shape emerges.

The foregoing observations apply equally to the $A = 0.8$ and DNS results, reflecting the absence of any identifiable qualitative differences between them. Quantitative differences could be at least partly attributable to finite-Reynolds-number effects. In this regard, the Taylor-scale Reynolds number of the DNS case is 300. Although HiPS k range is necessarily finite, inertial-range Kolmogorov phenomenology is embedded by means of the prescribed k dependencies of the coefficients of the terms in equation A 2, (which is a Taylor expanded form of equation 3.2).

Figure 10 shows the HiPS results for $A = 0.8$ replotted in another format used in Scatamacchia *et al.* (2012) that extends the abscissa to smaller values. Slower-than-exponential decay of the large-r tails is seen. In contrast, the decay of the DNS profiles is slightly faster than exponential, with each profile transitioning abruptly to much faster decay. The DNS results in Scatamacchia *et al.* (2012), not shown here, suggest front-like propagation of the transition r values at a speed of the order of the root-mean-square velocity fluctuation of the turbulent flow field.
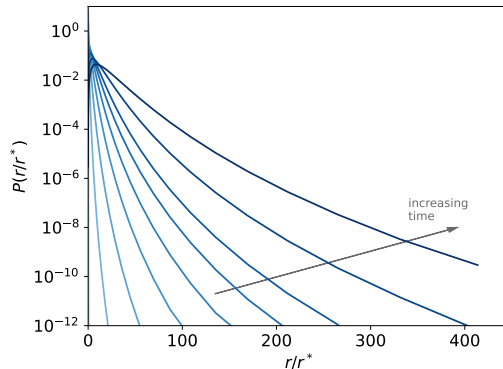
Figure 10: Dispersion PDFs for HiPS with $A = 0.8$, corresponding to figure 9b, for the same times as in that figure but omitting the initial condition.

It is reasonable that this quantity would set a bound on the rate of increase of r, but HiPS does not obey this constraint.

This reflects a model artifact noted by Shraiman & Siggia (1994) in a different context. Models that represent turbulent stirring as instantaneous fluid rearrangements occurring at Poisson-sampled times are subject to the large-deviation statistics of the Poisson process. These include a finite probability of any arbitrarily large excess of separations relative to approaches of parcel pairs in a given finite time. Figure 10 reflects the Poisson large-deviation statistics, which are not subject to any prescribed constraint on the magnitude of the implied flow velocity.

The root cause of the artifact is the Markovian nature of the time advancement, devoid of any constraint on future event occurrences based on past history. The remedy is to introduce history effects. Indeed, this is the distinguishing feature of flow HiPS that is lacking in mixing HiPS. This illustrates the potential benefits of merging the present extensions of mixing HiPS into flow HiPS in order to maximize the range of capabilities that are provided within a unitary framework. This point is elaborated in section 5.

The results for $A = 0.5$ exhibit the expected features. Unphysically high diffusivity relative to drift causes excessive probability flux toward low r values. The relatively short viscous-range time scale results in rapid equilibration as evidenced by convergence toward a low-k plateau corresponding to stationarity for this effectively one-dimensional case. The model results bear little resemblance to the DNS.

3.3.5. *Perspectives on A dependence*

All indications thus far are that HiPS with $A = 0.8$ is more useful for fundamental investigations of turbulence phenomenology than $A = 0.5$. The strong qualitative as well as quantitative sensitivity to variation of A is largely due to A dependence of the effective dimensionality of the model.

These observations imply that the time history of a single parcel pair for $A = 0.5$ that is shown in figure 6d exhibits an unphysically high frequency of excursions toward low separation values. In any case, that time trace highlights the degree of fine-grained detail that the model affordably captures, which can be useful in multi-physics studies notwithstanding the noted inaccuracies.

Moreover, the shortcomings of the choice $A = 0.5$ are not pervasive. HiPS with $A = 0.5$ is shown in what follows, and has been shown previously in other contexts (Kerstein 2014, 2021), to have considerable predictive capability with minimal empirical input. Other perspectives on A dependence are presented in Kerstein (2013), including cases in which variation of A modifies the effective dimensionality so as to change the flow configuration that is represented rather than the phenomenology of a particular flow.

Finally, examination of A dependence has value beyond the selection of the best value for a given purpose. In particular, Scatamacchia *et al.* (2012) describe the apparent log-normality of PDFs in figure 9c at small r as a non-trivial result. Present results impart a precise meaning to this characterization. Pair dispersion phenomenology has been shown here to be broadly encompassed by the drift-diffusion paradigm. This in itself does not ensure that pairs with viscous-range separations remain isolated in the viscous range long enough to develop log-normal statistics, nor that this isolation is insufficient to drive the system to equilibrium. In other words, the log-normal regime is an intermediate condition between two possible extremes. The differences between figure 9a and 9b show that the relative strengths of drift and diffusion are determinative in this regard and that quantifying this relationship on the basis of Lundgren's theory reproduces the small-r DNS features. Beyond that, the initial conditions are obviously influential, as confirmed by other HiPS results (not shown).

3.4. *Turbulent flux and diffusivity*

The turbulent diffusivity D_T is defined in relation to the turbulent scalar flux f using a Boussinesq assumption,

$$f = \langle \mathbf{u}'\phi' \rangle = -D_T \nabla \langle \phi \rangle, \tag{3.8}$$

where $\mathbf{u}'$ is a velocity fluctuation (used in the definition for reference to standard treatments) and ϕ' is the scalar fluctuation. ϕ' is referenced to the local mean, which is different in the two half-trees for the jump-periodic case of present interest.

HiPS formulation obeys equation 3.8 by construction with D_T evaluated as follows. HiPS eddy events can be considered in the context of a random walk, for which the diffusivity is $D_T = L^2/2\tau$, where L is the parcel displacement for each event, and τ is the time between events. The turbulent flux happens at the scale of the scalar gradient, as noted in section 3.1, so that turbulent flux is due to level-0 eddies, for which the parcel displacement is $L = L_0/2$. The mean time between parcel displacements is $\tau = 2\tau_0$ since only half the parcels are displaced during a given event. This then gives

$$\frac{D_T}{L_0^2/\tau_0} = \frac{1}{16} \tag{3.9}$$

as the dimensionless turbulent diffusivity. The corresponding dimensionless flux is

$$\frac{f}{L_0 \Delta\phi_0/\tau_0} = -\frac{1}{8}, \tag{3.10}$$

where $\nabla \langle \phi \rangle / (\Delta\phi_0/L_0) \equiv G = 2$ is used.

This flux (and so the corresponding D_T) was verified directly in the HiPS implementation by considering the scalar flux from the left half-tree to the right,

corresponding to flux across the domain center. This is calculated as

$$f = \frac{d}{dt} \sum_{i \in I_R} \phi_i L_{p,i} = \frac{L_0}{2} \frac{d}{dt} \langle \phi \rangle_R, \tag{3.11}$$

where I_R are the set of parcels in the right half-tree, $\langle \phi \rangle_R$ is the mean scalar value in the right half-tree, and $L_{p,i}$ is the parcel size. Changes to $\langle \phi \rangle_R$ are accumulated during the simulation as level-0 swaps occur and then divided by the run time to get $d\langle \phi \rangle_R/dt$. Only half the level-0 swaps are considered since half correspond to flux across the domain center of interest and half correspond to flux across the jump-periodic boundary.

Appendix B shows an exact calculation of the flux for a three-level tree, illustrating the possible states obtained.

3.5. *Production and dissipation*

In homogeneous turbulence, the scalar variance $\langle \phi'^2 \rangle$ is given by

$$\frac{\partial \langle \phi'^2 \rangle}{\partial t} = -2\langle \mathbf{u}' \phi' \rangle \cdot \nabla \phi - 2D \langle \nabla \phi' \cdot \nabla \phi' \rangle = \mathcal{P} - \langle \chi \rangle. \tag{3.12}$$

The right-hand side of this equation gives the difference between the mean scalar-variance production $\mathcal{P}$ and the mean scalar-variance dissipation rate $\langle \chi \rangle$ (Yeung & Sreenivasan 2014).

HiPS does not have a continuous physical domain, so calculation of production and dissipation using the standard definitions cannot be done directly. In addition, there is no physical diffusivity D defined in the HiPS tree, and micromixing is implemented phenomenologically. However, mean production and dissipation can be evaluated based on their roles as a scalar-variance source and sink, respectively.

Using $\mathcal{P} = -2\langle u'\phi' \rangle \cdot \nabla \phi$ from equation 3.12, the first equality in equation 3.8, equation 3.10, and $\nabla \phi = 2\Delta\phi_0/L_0$ gives the nondimensional production as

$$\frac{\mathcal{P}}{(\Delta\phi_0)^2/\tau_0} = \frac{1}{2}. \tag{3.13}$$

At steady state, production and dissipation balance and we have

$$\frac{\langle \chi \rangle}{(\Delta\phi_0)^2/\tau_0} = \frac{1}{2}. \tag{3.14}$$

These values were verified in HiPS simulation as follows. Production occurs due to level-0 eddies that transport fluid across the mean scalar gradient. In each half-tree, $\mathcal{P}$ is computed as the running sum of the difference in scalar variance before and after level-0 eddy events, divided by the simulation time. The values in each half-tree are then averaged. Recall that level-0 eddy events do not change the scalar values of individual parcels. The mean dissipation is computed similarly. In each half-tree, the running sum of the difference in scalar variance before and after eddies resulting in micromixing is computed, and this sum is then divided by the simulation time. The average in the two half-trees is computed.

Appendix B shows an exact calculation of the production and dissipation for a three-level tree.

The PDF of the scalar dissipation rate can also be evaluated. We present two approaches for its computation. The first approach makes use of the standard definition of χ given above in equation 3.12. The gradient $\nabla \phi'$ is computed as

(a)   (b)
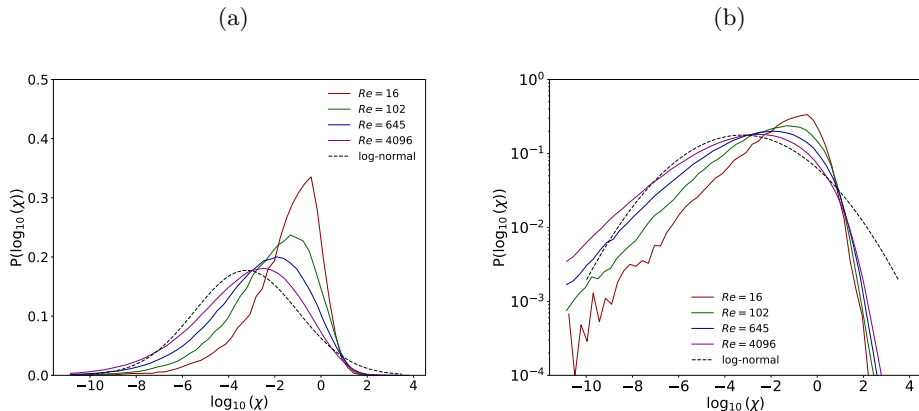
Figure 11: For $Sc = 1$, PDF of the scalar-variance dissipation rate for several Re, shown in (a) semi-log and (b) log-log coordinates. The dashed curve is a log-normal distribution with mean and variance corresponding to the $Re = 4096$ case.

$\Delta\phi/l^*$, where $\Delta\phi$ is the difference in scalar value between two neighboring parcel pairs. The diffusivity D is not considered directly, rather, χ is scaled so that $\langle\chi\rangle = \int \chi' P(\chi')d\chi'$, where $\langle\chi\rangle$ is evaluated as described above.

The second approach computes χ using the following scaling: $\chi = 2D\nabla\phi'\cdot\nabla\phi' \sim (\Delta\phi)^2/\tau$. Here, τ is a time scale between the micromixing events. In HiPS, we take τ to be the time since the last change of the parcel state due to micromixing events and denote this as τ_{tlc}. The $\Delta\phi$ is computed as $\tilde{\phi}-\hat{\phi}$, where $\tilde{\phi}$ and $\hat{\phi}$ are the scalar value of a given single parcel before and after an eddy event, respectively. $P(\chi)$ is then constructed, and we apply the same χ scaling as used in the first approach. It is found that these two approaches give nearly equal results.

In the sections below, we present the dissipation PDF using the second approach to compute χ and examine the impact of variations in the Reynolds and Schmidt numbers.

3.5.1. *PDFs of scalar-variance dissipation rate*

Figure 11 shows the PDF of $\log_{10}(\chi)$ for $Sc = 1$ at four Re of 16, 102, 645, and 4096, which correspond to trees with 6, 8, 10, and 12 levels, respectively. Results are presented on both log and linear scales. The mean dissipation rate scales as $1/\tau_0$, and is constant. As Re increases, the width of the PDF increases and the peak shifts to lower $\log_{10}(\chi)$ values. This is consistent with the fixed values of L_0 and τ_0, while the number of tree levels increases with increasing Reynolds number, which effectively introduces a wider range of scales into the system, and correspondingly broader PDFs.

PDFs of $\log_{10}(\chi)$ are shown in figure 12 for nine Schmidt numbers. A fixed Re of 256 is used, corresponding to a tree with nine levels and $i^* = 6$. The Sc numbers explored are 0.025, 0.063, 0.16, 0.4, 1, 4, 16, 64, and 256, corresponding to Δi of -4, -3, -2, -1, 0, 1, 2, 3, and 4, respectively. Results are presented on linear and log scales. For $Sc \leqslant 1$, as Sc increases the PDF broadens and the peak decreases and moves to lower $\log_{10}(\chi)$. Conversely, for $Sc > 1$, the PDFs show very little variation and effectively collapse. The behavior of these PDFs is largely dependent on the τ_s^*. For $Sc \leqslant 1$, τ_s^* increases with decreasing Sc as the

(a) (b)
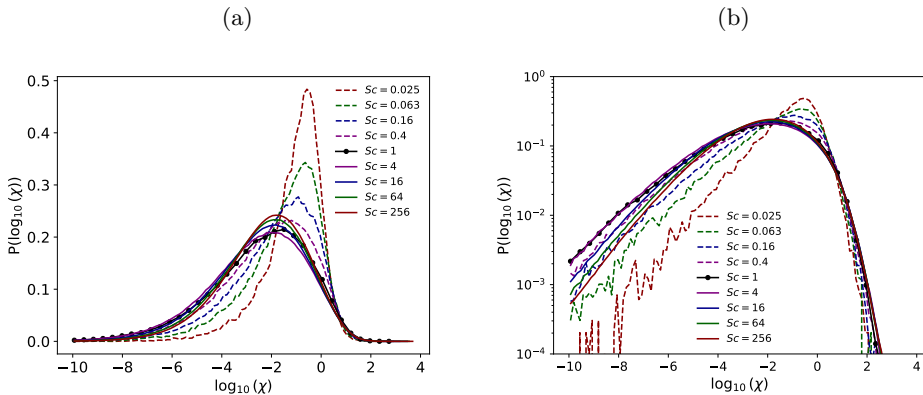
Figure 12: For $Re = 256$, PDF of the scalar-variance dissipation rate for several Sc, shown in (a) semi-log and (b) log-log coordinates.

scalar length scale corresponds to lower level indices, resulting in the variation of the PDFs. For $Sc > 1$, τ_s^* is constant at τ^*, and the PDFs are nearly identical.

This behavior is elaborated with additional simulations. Figure 13 is a schematic of the cases considered. Tree levels are indicated by short black dashes, and i^* and i_s^* are shown in blue and red, respectively. Quadrants a and b of the figure have $Sc \leqslant 1$, and quadrants c and d have $Sc \geqslant 1$. Quadrants a and c have constant i^* (const Re), corresponding to the cases shown in figure 12. Note that, as figure 13c for $Sc \geqslant 1$ shows, i_s^* varies, but τ_s^* is constant since $\tau_s^* = \tau^*$. Quadrants b and d show Re dependence for constant i_s^*.

Figure 14a shows simulations in which τ_s^* is constant, corresponding to figure 13b and c, and the PDFs show a strong collapse, especially for $Sc \leqslant 1$. For completeness, figure 14b shows the PDFs corresponding to figure 13a and d, for which τ_s^* varies for both $Sc \leqslant 1$ and $Sc \geqslant 1$. In this case, variations of the PDFs with Sc are evident for all Sc values.

The shapes of the PDFs shown in the figures are approximately log-normal. The log-normality of the kinetic energy dissipation rate was originally postulated in the pioneering work of Obukhov (1962) and Kolmogorov (1962). Gurvich & Yaglom (1967) presented an analysis arguing for log-normality of "some local non-negative characteristic of turbulence. . . defined only by the small-scale turbulent fluctuations (for example, the square of any space derivative of some hydrodynamic field," e.g., the scalar-variance dissipation rate. The HiPS simulations are not exactly log-normal and show some negative skewness. Figure 11b includes a log-normal distribution with mean and variance corresponding to the $Re = 4096$ case as the dashed curve. The negative skewness is particularly evident in figure 11b with the plot with P on a log scale. A very similar PDF shape was reported by Kerstein (1991) in simulations using the linear eddy model (LEM). Su & Clemens (2003) presented experimental scalar-variance dissipation-rate PDFs in planar jets. They noted the negative skewness and offered several possibilities for the departure from log-normality, including effects of the jet outer boundary, the moderate Reynolds number of the data, and effects of noise and resolution. These effects were analysed and discussed with the authors noting that "it appears that a slight negative skewness is a property of the scalar dissipation PDF."

The departure from log-normal behavior has been studied in detail. For example, Holtzer & Siggia (1994) studied passive scalar mixing in two dimensions and

const i^* (const Re)   const i_s^*

Δi 0   -1   -2   -3   0   -1   -2   -3

(a)

$Sc \leqslant 1$ i^*, i_s^* ... (schematic tree)

(b)

Δi 0   1   2   3   0   1   2   3

$Sc \geqslant 1$

(c)   (d)

Figure 13: Schematic of simulations with varying Sc and Re. Short dashes correspond to tree levels, with i^* and i_s^* indicated. Sc depends on Δi. $Sc \leqslant 1$ for (a) and (b); and $Sc \geqslant 1$ for (c) and (d). In (a) and (c), i^* is constant and i_s^* varies. In (b) and (d), i_s^* is constant and i^* varies. The Reynolds number depends on i^*.

(a)   (b)

Figure 14: PDF of scalar-variance dissipation rate for (a) constant τ_s^*, (b) variable τ_s^*.

Figure 15: PDF of scalar-variance dissipation corresponding to figure 14 for
Sc=1 and Sc=256 plotted on coordinates for comparison to Chertkov *et al.*
(1998) for the scaling of the high χ tail. The Sc=1 curves have been shifted by
2.5 vertical-axis units for clarity.

found good agreement with experimental data in more complex configurations.
They show that a stretched exponential function fits the dissipation PDF in
the large dissipation tail. Chertkov *et al.* (1998) studied scalar advection using
the Kraichnan (1974) model at high Schmidt number. They derived an analytic
expression for the dissipation PDF, which can be represented as $\log(P(\chi)\chi^{1/2}) \propto$
$\chi^{1/3}$. For $\chi \gg \langle\chi\rangle$, the PDF is given by a stretched exponential, with $\log P(\chi) \propto$
$\chi^{1/3}$.

Figure 15 shows $\log_{10}(P(\chi)\chi^{1/2})$ and $\log_{10}(P(\chi))$ versus $\chi^{1/3}$ for HiPS with
$Sc = 1$ and $Sc = 256$ (corresponding to figure 14a). Note that the $Sc = 1$ curves
have been shifted by 2.5 vertical-axis units for clarity. (Without the shift they
collapse with the Sc=256 curves.) In addition to the HiPS data, linear fits through
the 12 largest χ values are shown, which correspond to the fit to Chertkov's model
in the coordinates plotted. It is seen that for both Schmidt numbers, the HiPS
data reproduces the predicted 1/3 exponent. Moreover, the fit is better when the
subdominant $\chi^{1/2}$ factor is included, indicating at least the possibility that the
model captures this dependence.

There is prior empirical support for the 1/3 exponent for $Sc = 1$ as well as
high Sc although the theory is specific to the high-Sc Batchelor regime (Chertkov
et al. 1998). No existing model or analysis has explained the $Sc = 1$ result beyond
speculative proposals and the broad observation that "stretched-exponential tail
is natural for steady PDF of the gradients" (Chertkov *et al.* 1998).

These authors also note that the phenomenology "is determined by the dy-
namics of stretching (not of rotations), thus it is likely to take place in any
dimensions." This could explain the accuracy of the $A = 0.5$ HiPS simulation
despite the caveats noted earlier. A related point discussed in Appendix A is
that the shape of the HiPS viscous-range pair-separation PDF is qualitatively
independent of A, perhaps reflecting the validity of the corresponding theoretical
result (Lundgren 1981) for any spatial dimension.

3.6. *Scalar spectra*

Scalar transport in turbulent flow is commonly represented and analyzed using the scalar energy spectrum. A detailed interpretation of the scalar energy spectrum in the context of HiPS was provided by Kerstein (2013) but no computations were performed. Here we provide a summary description and computations of the scalar spectrum for various Schmidt numbers.

In HiPS, the energy spectra are inferred from the differences of scalar variances at adjacent levels of the tree. As noted by Kerstein (2013), the quantity $\int_k^\infty E(k')dk'$ "scales as the variance of scalar fluctuations associated with wavenumbers exceeding k." The tree structure of HiPS has discrete, geometrically decreasing length scales with increasing tree level. We can think of each level i of the tree as having a corresponding wavenumber k_i with $l_i = 2\pi/k_i$. The scalar variance in a given subtree at level i is computed as the variance of the parcels in that subtree, that is, $\langle(\phi - \langle\phi\rangle_i)^2\rangle$, where $\langle\phi\rangle_i$ is the average over parcels in the given subtree at level i. This variance is then ensemble averaged over all subtrees of the given level and over all flow realizations (or time samples in statistically stationary cases), and is denoted $\mathrm{var}_i\phi$. The subtree quantity $\langle\phi\rangle_i$ is a filtered quantity "such that fluctuations at wavenumbers greater than k have been removed" (Kerstein 2013). A discrete scalar spectrum is then given by

$$E(k_i) = \frac{\mathrm{var}_i\phi - \mathrm{var}_{i+1}\phi}{k_{i+1} - k_i}. \tag{3.15}$$

As A approaches unity, this converges to the familiar continuum relationship between the scalar spectrum and the variance of the filtered scalar field, assuming spectrally sharp filtering.

Scalar spectra are obtained for three mixing regimes: inertial-advective, inertial-diffusive, and viscous-advective. Figure 16 shows scalar spectra from HiPS simulations over a range of Schmidt numbers.

The inertial-advective regime is characterized by turbulent scalar transport with negligible diffusive effects and spectral transfer from large to small scales is governed by the scalar-variance dissipation rate χ, which is independent of the length scale. The increasing advective rate with decreasing length results in quasi-stationary behavior that responds quickly to energy transferred from larger scales. In this regime, time scales are related to length scales as $\tau \sim l^{2/3}$ and the kinetic-energy spectrum exhibits $k^{-5/3}$ scaling. In HiPS, this time scale-length scale relationship is imposed, but as Kerstein (2013) notes "scalar cascading in HiPS is an outcome rather than a prescribed behavior, so the nature of that cascading in HiPS must be ascertained."

It is seen that HiPS does in fact exhibit the -5/3 wavenumber power-law of the scalar spectrum. While HiPS does not prescribe the cascading behavior, its formulation is consistent with it, as HiPS subsumes the key phenomenology that governs it. This is evident as HiPS eddies result in local scale reduction, the eddy rate increases with decreasing level length giving quasi-stationary behavior, and the HiPS eddies are non-dissipative at all scales greater than l^*.

Figure 16a shows simulations for scalars with $Sc \geqslant 1$. Six Sc values are included. These have $Sc = 1, 4, 16, 64, 256, 1024$, corresponding to integer values of $\Delta i = i_s^* - i^*$ from 0 to 5, (see equation 2.21). The simulation has a total of 12 levels and $i^* = 4$. This accommodates both a significant wavenumber range of the inertial-advective regime and extension to smaller scales ($i > i^*$) for $Sc > 1$. The
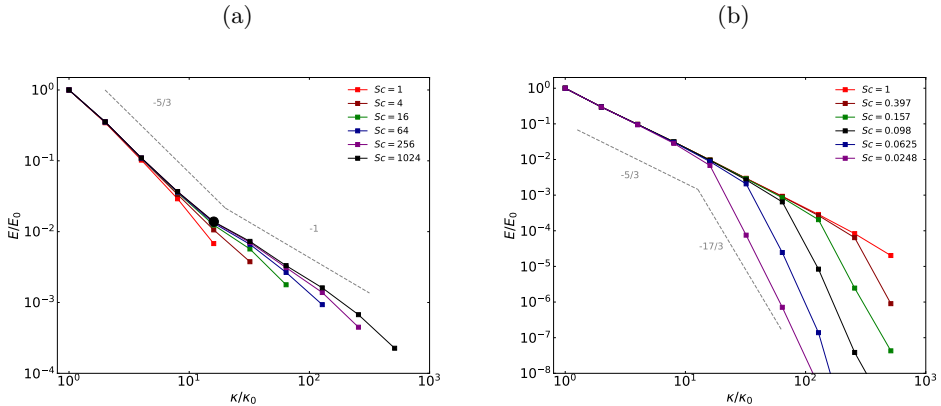
Figure 16: Scalar energy spectra for (a) $Sc \geqslant 1$, and (b) $Sc \leqslant 1$.

simulations were run for $t = 1000\tau_0$, and flow states spaced by time intervals τ_0 were processed beginning with $50\tau_0$.

All spectra show a clear transition between the inertial-advective regime and the viscous-advective regime and they all obey the $-5/3$ scaling at low wavenumbers. In the viscous-advective regime $i > i^*$, the spectra show the expected k^{-1} scaling. This is most obvious for the scalars with the highest Sc. As the micromixing/dissipation level i_s^* is reached, the energy spectrum steepens slightly relative to the nominal k^{-1} scaling, reflecting spectral backscatter caused by swap-induced separation of subtree pairs that transfers spectral intensity to larger scales. In this regard, analysis of spectral fluxes in HiPS is a promising future undertaking.

In the simple micromixing model used in this study, immediately after a swap occurs at level i_s^*, all parcels in the left subtree of the node at the given eddy level are mixed to their mean value in that subtree; all parcels in the right subtree are similarly mixed. This results in no scalar variance among parcels at levels greater than i_s^*, so the scalar energy spectrum becomes effectively chopped at length scales below l^*, corresponding to levels $i > i_s^*$. As formulated, this eliminates the need to implement any eddy events at levels $i > i_s^*$ because they would have no effect.

This, however, provides an inadequate representation of the inertial-diffusive scaling range, for which Batchelor (1959) predicted a $-17/3$ spectral scaling. This scaling has only recently been demonstrated by Yeung & Sreenivasan (2013, 2014) using DNS due to the difficulty of experiments and computational cost of DNS.

Accordingly, the $Sc < 1$ eddy event, which performs the described mixing if the event level is i^*, is modified in order to approximate the theoretical spectral scaling in lieu of the sharp cutoff at level i_s^*. Instead of assuredly mixing the respective two subtrees of the level-i^* event apex, for any eddy event at level $i \geqslant i^*$, both the left and right subtrees of the event apex are individually mixed with probability p based on a Bernoulli trial. This allows scalar fluctuations to persist below the Obukhov-Corrsin scale. At level $j > i_s^*$, we then have an inhomogeneous scalar fraction q^j where $q = 1 - p$. The scalar variance then would be q^j times what it would be in a $-5/3$ spectrum. Here it is assumed that the inertial-advective cascade proceeds as usual in the successive generations of unmixed subtrees, which requires the re-introduction of eddy events at levels $j > i_s^*$ where such events can change the system state (versus the absence of such

events for $q = 0$). Recalling that spectral amplitude scales in proportion to the scalar variance, the -17/3 power-law spectrum scaling is obtained by imposing the requirement

$$\frac{E_j}{E_{i_s^*}} = \frac{\mathrm{var}_j \phi}{\mathrm{var}_{i_s^*} \phi} = q^j \left(\frac{k_j}{k_{i_s^*}} \right)^{-5/3} = \left(\frac{k_j}{k_{i_s^*}} \right)^{-17/3}. \tag{3.16}$$

Now, $l_s^*/l_j = 2^j$, so $k_j/k_{i_s^*} = 2^j$, and $j = \log_2(k_j/k_{i_s^*})$. Using this and solving the above equation for q gives $q = 2^{5/3-17/3} = 0.0625$ and $p = 1 - q = 0.9375$. This result is approximate because it is based on strict mean-field Kolmogorov phenomenology, omitting fluctuation effects such as backscatter (discussed with reference to the viscous-advective regime) that are inherent to HiPS.

On this basis, figure 16b shows simulation results for $Sc < 1$ in the inertial-diffusive regime. Each case again includes 12 tree levels and was run for the same time with the same number of flow states processed as the cases shown in figure 16a. That figure had $i^* = 4$ for $Sc = 1$, with higher levels accommodating larger Sc. For $Sc < 1$ in figure 16b, $i^* = 9$ for $Sc = 1$ (with levels starting at 0), and $Sc = 1, 0.397, 0.157, 0.0625, 0.0248$, and 0.098 (rounded), corresponding to $\Delta i = i_s^* - i^*$ from 0 to -5, respectively. The slopes of scalar spectra in the inertial-diffusive regime are approximately -17/3, with some statistical variation present. The slope in the inertial-diffusive regime is slightly steeper than -17/3, but it can be brought into agreement with this exponent by using a slightly lower value of p (around 0.9).

The scalar spectra discussed above and plotted in figure 16 are discrete. As an alternative formulation, we can evaluate continuous spectra in the inertial-advective regime, which is convenient for analysis. This is done using a power-law with an exponent of $-5/3$, consistent with the presented spectra. The power-law amplitude is set so that the integral of the continuous spectra, extending to level 1 corresponding to L_I, recovers the total variance. Using such continuous spectra, we next denote the compensated spectrum $Ek^{-5/3}$ as E_{k53}; its nondimensional value is

$$\frac{E_{k53}}{\Delta\phi_0^2/L_0^{2/3}} = 4.3. \tag{3.17}$$

This is based on a simulation with $N = 12$ levels and $Sc = 1$, but applies generally given the collapse of the scalar spectra in the inertial-advective range, evident in figure 16.

4. Empirical correspondence

In this section we relate HiPS quantities to their physical counterparts. Given reference scales L_0, τ_0, and $\Delta\phi_0$, a HiPS simulation is defined in terms of the Reynolds and Schmidt numbers from equations 2.2 and 2.20, respectively, and the dimensionless scalar gradient G:

$$Re = \left(\frac{L_0}{l^*} \right)^{4/3} = A^{-\frac{4}{3}i^*}, \tag{4.1}$$

$$Sc = (l^*/l_s^*)^{p_s}, \tag{4.2}$$

$$G = \frac{\nabla\phi}{\Delta\phi_0/L_0}. \tag{4.3}$$

All other dimensionless quantities will be functions of Re, Sc, and G. Note that specifying i^* is equivalent to specifying Re, and that the number of levels needed to resolve a $Sc = 1$ scalar is $N = i^* + 3$. Given Re and Sc, we then have l^* and l^*_s.

In previous sections we evaluated the mean scalar-variance dissipation rate, normalized turbulent diffusivity, and amplitude of the compensated inertial-range spectrum. They are reproduced here for convenience, and denoted C_χ and C_D, and C_E, respectively:

$$\frac{\langle\chi\rangle}{\Delta\phi_0^2/\tau_0} = C_\chi = \frac{1}{2}, \tag{4.4}$$

$$\frac{D_T}{L_0^2/\tau_0} = C_D = \frac{1}{16}, \tag{4.5}$$

$$\frac{E_{k53}}{\Delta\phi_0^2/L_0^{2/3}} = C_E = 4.3. \tag{4.6}$$

Next, three coefficients C_ϵ, C_η, and C_s are evaluated, each of which incorporates an empirical datum such that, combined with the three coefficients above, the physical quantities that define particular flow cases are fully specified.

The scalar spectrum has the model form $E(k) = \beta\langle\chi\rangle\epsilon^{-1/3}k^{-5/3}$. Solving this for the kinetic energy dissipation rate ϵ and using $\beta = 0.7$ as the Obukhov-Corrsin constant (Gotoh & Watanabe 2015; Donzis *et al.* 2010) gives

$$\frac{\epsilon}{L_0^2/\tau_0^3} = \left(\frac{\beta\langle\chi\rangle}{E_{k53}}\right)^3 / \frac{L_0^2}{\tau_0^3} = C_\epsilon = 0.000539. \tag{4.7}$$

Donzis *et al.* (2010) performed DNS of passive scalar mixing in homogeneous turbulence with a mean scalar gradient, corresponding to the HiPS simulations considered here. They report a sharp transition from inertial-advective to viscous-advective spectrum scaling at $k^*\eta \approx 0.05$, where $\eta = (\nu^3/\epsilon)^{1/4}$ and $k^* = 2\pi/l^*$. Using these relations, along with $\tau_\eta = \eta^2/\nu$, gives

$$\frac{l^*}{\eta} = C_\eta = 126, \tag{4.8}$$

$$\frac{\eta}{L_0} = Re^{-3/4}C_\eta^{-1}, \tag{4.9}$$

$$\frac{\nu}{L_0^2/\tau_0} = Re^{-1}C_\epsilon^{1/3}C_\eta^{-4/3}, \tag{4.10}$$

$$\frac{\tau_\eta}{\tau_0} = Re^{-1/2}C_\epsilon^{-1/3}C_\eta^{-2/3}. \tag{4.11}$$

Three common definitions of the physical Reynolds number are denoted here as $\hat{Re}$, $\tilde{Re}$, and $\breve{Re}$. These are defined below and related to the HiPS Reynolds

number Re:

$$\hat{Re} = \left(\frac{L_0}{\eta}\right)^{4/3} = C_\eta^{4/3} Re, \tag{4.12}$$

$$\tilde{Re} = \frac{L_0^2}{\tau_0 \nu} = C_\eta^{4/3} C_\epsilon^{-1/3} Re = C_\epsilon^{-1/3} \hat{Re}, \tag{4.13}$$

$$\breve{Re} = \frac{\nu_T}{\nu} = \frac{Pr_T D_T}{\nu} = Pr_T C_D C_\epsilon^{-1/3} C_\eta^{4/3} Re = Pr_T C_D C_\epsilon^{-1/3} \hat{Re} = Pr_T C_D \tilde{Re}. \tag{4.14}$$

Here, ν_T is a turbulent viscosity and is related to D_T by the turbulent Prandtl number Pr_T, for which an empirical value can be used, e.g., $Pr_T = 0.85$ (Li 2019; Churchill 2002).

Donzis $et~al.$ (2010) showed excellent agreement between their DNS data and Kraichnan's model (Kraichnan 1968) for the scalar power spectrum in the dissipative roll-off range,

$$\frac{Ek\eta_b}{\langle\chi\rangle\tau_\eta\eta_b} = \frac{C_b(1 + \sqrt{6C_b}k\eta_b)}{\exp(\sqrt{6C_b}k\eta_b)}. \tag{4.15}$$

This equation extends an analysis by Batchelor to account for fluctuations of strain rate magnitude. Donzis $et~al.$ (2010) report values of the Batchelor constant, C_b, of 4.93 and 4.52 for Schmidt numbers greater and less than one, respectively. An average value of $C_b = 4.725$ is taken here. At low $k\eta_b$, equation 4.15 corresponds to the inertial-advective range with slope k^{-1}, and the right-hand side of the equation is C_b. The HiPS spectrum in the inertial-advective range has a slope of k^{-1} and a sharp cutoff at $k_s^* = 2\pi/l_s^*$. We relate k_s^* to η_b by integrating equation 4.15 from zero to infinity and equating it to $C_b k_s^*$. This gives

$$\frac{l_s^*}{\eta_b} = C_s = \pi\sqrt{6C_b}. \tag{4.16}$$

From the definitions of the Reynolds and Schmidt numbers we have

$$\frac{l_s^*}{L_0} = Re^{-3/4} Sc^{-1/p_s}. \tag{4.17}$$

The physical Schmidt number corresponding to $Sc = (l^*/l_s^*)^{p_s}$ is given by

$$\hat{Sc} = \left(\frac{\eta}{\eta_s}\right)^{p_s} = \left(\frac{C_s}{C_\eta}\right)^{p_s} Sc. \tag{4.18}$$

Using $\hat{Sc} = \nu/D$ and equation 4.10 then gives an expression for the scalar diffusivity

$$\frac{D}{L_0^2/\tau_0} = C_\epsilon^{1/3} C_\eta^{p_s-4/3} C_s^{-p_s} Re^{-1} Sc^{-1}. \tag{4.19}$$

5. Incorporation of Sc dependence into the HiPS flow formulation

5.1. Adaption of the new features to the flow-HiPS framework

The present study focuses on incorporation of Sc dependence into the HiPS mixing formulation that was introduced in Kerstein (2013). This formulation

time advances advected scalar fields based on prescribed swap-sampling rates. An alternative HiPS formulation that instead advances velocity components was proposed in Kerstein (2013) and has been applied to several representative cases Kerstein (2013, 2014, 2021). In this flow simulation, the instantaneous flow state within in each subtree determines the time scale τ of the node at the apex of the subtree. τ values thus vary from node to node at a given level and all τ values are time dependent.

The flow-state dependence of τ values is specified much as in the one-dimensional turbulence (ODT) model (Kerstein 2022; Chen *et al.* 2024). On this basis, flow HiPS embodies a more detailed physics representation than mixing HiPS in the same sense as ODT relative to the LEM (Kerstein 1991).

While LEM has proven widely useful for subgrid mixing closure as well as standalone studies of nonreacting and reacting turbulent scalar mixing (e.g., Zimberg *et al.* 1998; Echekki 2008; Oevermann *et al.* 2008), ODT has been extended by incorporating scalar fields and reaction mechanisms to provide a more detailed mixing treatment (e.g., Hewson & Kerstein 2001; Lignell *et al.* 2015; Goshayeshi & Sutherland 2015; Klein *et al.* 2023). For the same reason, such extensions of flow HiPS should also be useful. Therefore a brief conceptual outline of the extension of flow HiPS to incorporate the scalar advection and mixing phenomenology introduced in the present study is provided. For this purpose, multiplicative coefficients are omitted. They can be evaluated using adaptations of the approach introduced in section 4. Additionally, the method used to convert from discretized levels to a continuum of length scales remains the same, so it is not discussed further.

This extension requires flow HiPS to be implemented using the extended tree structure that includes the viscous regime. Now the transition from inertial to viscous-dissipative phenomenology is no longer prescribed, and instead must be evaluated on the fly as follows. Along any path downward from the apex of the tree, the first node whose associated eddy viscosity is less than the kinematic viscosity is deemed to be viscosity-dominated, so that node and the entire subtree emanating from it are deemed to have the same τ value as the current value at the node.

As noted in section 2.4, l_s^* is the scale at which molecular and eddy diffusivities balance, analogous to the inertial-to-viscous transition criterion. Now this criterion for the determination of l_s^* is applied on a local instantaneous basis rather than using the standard evaluation of l_s^* based on Kolmogorov phenomenology. Again, this is determined by following each path downward from the apex until a node is encountered that satisfies the criterion. Its associated subtree is possibly or certainly, depending on Sc (see section 3.6), fully homogenized whenever a swap results in inhomogeneity.

For $Sc < 1$, this is a precise application of the stated criterion. For $Sc > 1$, l_s^* is in the viscous range, so there is no size-l_s^* eddy whose effective diffusivity can be compared to the molecular diffusivity. Instead, a time-scale balance is enforced. The strain rate $1/\tau$ associated with a given viscous-range node is based on the local instantaneous τ value corresponding to inertial-to-viscous transition along the unique path from the tree apex to the node. Thus, there is an indirect eddy-viscosity influence owing to the transition criterion. For the given node, at some level l, the associated molecular-diffusive time scale is l^2/D. Accordingly, $l^2/D < \tau$ is the criterion for identifying a node whose associated subtree is

subject to homogenization with a specified probability whenever it deviates from homogeneity.

In flow HiPS, neither ν_T nor D_T is known by construction because eddy frequencies are not hardwired. However, the availability of the velocity field provides convenient relationships between the model Reynolds number and its physical counterpart. The ability to incorporate flow geometry leads to flow-specific Reynolds-number definitions, sometimes multiple definitions for a given flow configuration, so the model-to-physical Reynolds number conversion will generally be case-specific. Since molecular transport is a microphysical mechanism well within the universal range of flow scales, the Schmidt-number conversion formulated in section 4 should be applicable.

5.2. *History effects*

An anomaly of event-based representation of turbulent stirring governed by Poisson sampling of event occurrences is noted in section 3.3.4. The deficiency of Poisson sampling in this regard is the absence of history effects that might otherwise constrain the large-deviation statistics of these events. In flow HiPS, the flow field is the embodiment of the current influence of past history, and future events are sampled accordingly. To be clear, time advancement of flow HiPS as a whole is Markovian, but event sampling *per se* is dependent on the sequence of earlier events.

The main effect of this dependence is to cluster eddy events in time, potentially boosting whatever intermittency is inherent in mixing HiPS. The dependence can also be prescribed so as to limit the degree of clustering and suppress the noted anomaly.

The history effect in flow HiPS is Lagrangian in that the parcel state at a given tree location reflects interactions with its surroundings as it executed the trajectory that culminated in its current placement. This is reminiscent of the Lagrangian-history direct-interaction approximation (LHDIA) that substantially improved its antecedent, the DIA, as summarized by Zhao (2021).

6. Discussion and Conclusions

6.1. *Model extensions*

Hierarchical parcel swapping (HiPS) was originally introduced as a formulation designed to time advance unity-Sc diffusive scalar fields advected by parametrically specified inertial-range turbulence (Kerstein 2013), extensible to turbulent flow simulation by introducing a vector velocity field (Kerstein 2013, 2014). Here, extension to nonunity Sc has been achieved by means of two model extensions. For $Sc > 1$, the viscous regime has been incorporated by adopting the time scale of the smallest turbulent eddies as the advective time scale governing swap occurrences at all length scales below the inertial range, where such swaps idealize the viscous-range effects of the smallest inertial-range eddies rather than (nonexistent) smaller-scale eddies. On this basis, the HiPS tree has been extended to the Sc-dependent Batchelor scale η_b, at which each pair of adjacent parcels is mixed as needed to maintain compositional equivalence. For $Sc < 1$, the Obukhov-Corrsin scale exceeds the transition scale l^* from inertial to viscous flow scaling so mixing has been introduced within the subrange $[\eta_{oc}, l^*]$ of the inertial range. This generalizes the enforcement of the compositional uniformity

of parcel pairs to imposition of this requirement on larger subtrees. For any Sc, the HiPS tree can be extended as far down in scale as desired provided that compositional uniformity is enforced below scale l_b.

These model extensions serve two purposes. First, they are the basis for assessments and demonstrations of flow and mixing physics that are captured by the model. Second, they broaden the scope of scientific and practical applications of the model. Present contributions that fall within the respective categories are summarized.

6.2. *Physics investigations and results*

Notably in HiPS, the swaps alone, which are simply displacements of subtrees within the tree structure, have been shown to capture much of the phenomenology of parcel-pair dispersion within and across the viscous and inertial ranges. In particular, it has been shown that the multiplicative stride A of level-to-level scale breakdown is a physical parameter of the model in addition to its role as resolution adjustment. For pair dispersion, A controls the relative strengths of drift of the pair separation to higher values and diffusive broadening of the ensemble statistics of pair dispersion. For the viscous regime, the choice $A = 0.8$ has been shown analytically to match the theoretical result of Lundgren (1981) in this respect. This A value yields substantially better agreement with DNS results of pair-separation PDF evolution across the viscous and inertial ranges than the default value $A = 0.5$. The combination of mechanisms that produces this outcome has been diagnosed in detail.

The complementary physical and algorithmic roles of A impose a trade-off that is central to the present study. To span a scale range $\sigma \gg 1$, a HiPS tree with $N + 1$ levels is needed where $A^{-N} = \sigma$, so $N = \ln \sigma / \ln(1/A)$. Since 2^N parcels reside at the base of a level-$(N + 1)$ tree, the number of parcels scales as $\sigma^{\ln 2 / \ln(1/A)} \equiv \sigma^{d_{\mathrm{eff}}}$, which defines an effective dimensionality $d_{\mathrm{eff}} = \ln 2 / \ln(1/A)$ of the tree, analogous to the box-counting definition of fractal dimension. $A = 0.5$ is conceptually appealing in that it yields $d_{\mathrm{eff}} = 1$, which suggests an interpretation of HiPS as a representation of flow evolution along a line of sight through a three dimensional flow. This is both computationally efficient and, as previously shown (Kerstein 2014, 2021), it yields more accurate results than other A values for canonical planar-symmetric flow configurations. $d_{\mathrm{eff}} = 3$ corresponds to $A = 2^{-1/3} \approx 0.8$, a result that is derived in section 3.3.2 from a formally different but mathematically equivalent perspective. This result reinforces the advantage of $A = 0.8$ from a physics perspective, as definitively confirmed by the results shown in figure 9, while the alternate derivation directly quantifies the commensurately high computational cost with similar resolution requirements to DNS.

The overall picture that emerges is that there is not a single A value for which HiPS is physically consistent with all turbulence phenomenology of interest, but for a wide range of turbulence phenomenology encompassing previous as well as present analysis and applications of the model, physically consistent behaviors are obtained based on case-specific A values.

HiPS has been compared in this regard to LEM, which is less abstract in the sense that it is framed in physical space, albeit in one spatial dimension, rather than as a tree. The LEM eddy event is a triplet map that, as in HiPS, imposes multiplicative scale reduction. Both models also impose parcel-pair separation, but in LEM one such event can unphysically increase pair separation by a large

multiplicative factor. Consequently, LEM time advancement of $P(r)$ bears much less resemblance to the physical behavior than HiPS.

This introduces another trade-off that has been noted. On a fully resolved one-dimensional domain, LEM affordably accommodates accurate molecular transport coupled to chemical kinetics. The fidelity of the current extension of HiPS relative to LEM in this regard remains to be determined, but the present dispersion and mixing results demonstrate that more of the relevant phenomenology is captured than was originally anticipated in Kerstein (2013).

The computational efficiency of the choice $A = 0.5$, in conjunction with previous demonstrations of the predictive performance of the model for this A value, led its adoption in the present study of mixing properties. The scaling properties of the various spectral regimes have no intrinsic A dependence, so the reproduction of the known spectral scalings of the inertial-convective, inertial-diffusive, and viscous-advective regimes by the extended model is deemed to be robust.

It is noteworthy that the tail behavior of the PDF of scalar-variance dissipation is found to be in conformance with the high-Sc theoretical prediction of Chertkov *et al.* (1998), which is based on analysis of scalar intermittency induced by non-intermittent narrowband stochastic advection. This suggests that the associated phenomenology has a more abstract mathematical foundation than has previously been recognized. It is especially intriguing that HiPS yields the same tail shape for $Sc = 1$, which has been empirically demonstrated but not yet explained beyond speculative proposals (Chertkov *et al.* 1998). The HiPS result suggests a new avenue of investigation of inertial-range scalar intermittency.

This raises the broader question of the HiPS representation of inertial-range scalar intermittency more generally. A suggestive indication is that LEM has been shown to reproduce scalar structure-function exponents with reasonable quantitative accuracy (Kerstein 1991). This has been explained by an analysis (Kalda & Morozenko 2008) that suggests some commonality with the HiPS representation of inertial-range phenomenology. It has been suggested that LEM, and by implication HiPS, might embody a spurious intermittency mechanism for the case of an imposed mean scalar gradient owing to the Poisson sampling of event occurrence times (Shraiman & Siggia 1994). (Another anomaly resulting from Poisson sampling is noted in section 3.3.4.) For this reason, HiPS inertial-range scalar intermittency is best evaluated using a different flow configuration. This is beyond the present scope, so it will be addressed elsewhere.

6.3. *Capability development for applications*

DNS data has been used to calibrate coefficients that relate model scalar power spectrum amplitudes and transition wavenumbers to their physical counterparts. This will enable future quantitative application of the model to flow configurations of interest.

The extension to nonunity Sc enables model application to heat transfer with nonunity Pr and further model extension to reacting flows subject to differential diffusion effects. For these applications, it remains to be determined whether HiPS will have overall cost/performance advantages relative to the triplet-map-based methods LEM and ODT, whose resolution of scalar diffusion in 1D physical space is costly but provides high fidelity for combustion and related applications Chen *et al.* (2024).

The most important future extension of HiPS is incorporation of the newly

introduced features into flow HiPS (Kerstein 2014, 2021). This has the potential to remedy a particular anomaly that has been noted, but more importantly, to broaden the range of flow phenomena that can be amalgamated into a unitary modeling framework.

A feature that will facilitate the use of HiPS for applied studies is its formal resemblance to existing mixing models. In particular, subgrid-scale mixing closures of conventional under-resolved three-dimensional flow computations typically involve a collection of parcels that are mixed either pairwise or with the notional mean parcel composition (Fox 2003). Pairwise mixing can be based on random parcel pairings (Curl 1963) or pairing weighted by the similarity of parcel compositions (Subramaniam & Pope 1998). To the extent that time advancement of the PDF of parcel compositions is sufficient to close the flow computation, the role of HiPS would be to introduce turbulence phenomenology into the selection of parcel pairs to be mixed. Thus, the time-advancement operations need no modifications other than a different source of the inputs that specify which parcels should be selected to be mixed. This offers the prospect of a straightforward remedy for longstanding deficiencies of existing mixing closures (Fox 2003).

Declaration of Interests. The authors report no conflict of interest.

Appendix A. Analysis of the time advancement of the PDF of parcel-pair separation

To compare equation 3.2 to conventional representations of pair-dispersion statistics, that equation is approximated by treating k as continuous and Taylor expanding the right-hand side. First, equation 3.2 is multiplied by $2B^{1-k}$, giving

$$2B^{1-k}\frac{dP_k}{dT} = 2BP_{k-1} - (2+B)P_k + P_{k+1}. \tag{A 1}$$

Substitution of the Taylor expansion $P_{k\pm 1} = P_k \pm \left.\frac{dP_k}{dk}\right|_k + \frac{1}{2}\left.\frac{d^2 P_k}{dk^2}\right|_k$ into equation A 1 gives

$$2B^{1-k}\frac{\partial P_k}{\partial T} = (B-1)P_k - (2B-1)\frac{\partial P_k}{\partial k} + \left(B + \frac{1}{2}\right)\frac{\partial^2 P_k}{\partial k^2}. \tag{A 2}$$

(Note that in the Taylor expansion, the k-space interval $\Delta k = (k+1) - k = 1$ is used.) At this point the truncation of the expansion at second order is arbitrary but its validity is addressed in what follows.

Next, P_k is converted to the more conventional form $P(r)$ where r is the normalized physical-space parcel separation corresponding to level k. The probability in the k interval $\Delta k = 1$ is $P_k \Delta k = P_k$, which must equal the same probability expressed as $P(r)\Delta r$, where $\Delta r = r - Ar = (1-A)r$. Then $P_k = P(r)\Delta r/\Delta k$. As in equation 3.5, the parcel-pair separation is $Y_k = l^* A^{3-k}$. Normalizing this by Y_1, the nondimensional pair separation is $r(k) = A^{1-k} = \exp[(k-1)\ln(1/A)]$. Again treating k as continuous, $\Delta r/\Delta k$ is evaluated as $dr/dk = r\ln(1/A)$. On this basis, $P(r)$ is evaluated as $P_k/[r\ln(1/A)]$ for $k = 1 + (\ln r)/\ln(1/A)$.

For nonunity B, equation A 2 has no convenient general solution so investigation of inertial-range dispersion will be performed by numerical solution of equation A 1. That equation is specialized for application to the viscous range by setting B equal to unity, which has the same effect in equation A 2 as setting $\tau_k = \tau^*$ for all k. Importantly, this decouples B from its definition in terms of A. The underlying model still depends on $A < 1$ through the A dependence of the eventual conversion from k to r. On this basis, equation A 2 reduces to

$$\frac{\partial P_k}{\partial T} = -V\frac{\partial P_k}{\partial k} + D\frac{\partial^2 P_k}{\partial k^2}, \tag{A 3}$$

where $V = 1/2$ and $D = 3/4$.

The solution for $P_k(T = 0) = \delta(k - k_0)$ is

$$P_k = \frac{1}{(4\pi DT)^{1/2}} \exp\left[(k - k_0 - VT)^2/(4DT)\right], \tag{A 4}$$

which corresponds to log-normally distributed $P(r)$, namely

$$P(r) = \frac{1}{r(4\pi\hat{D}T)^{1/2}} \exp\left(\frac{[\ln(r/r_0) - \hat{V}T]^2}{4\hat{D}T}\right), \tag{A 5}$$

where $r_0 = r(k_0)$, $\hat{V} = V\ln(1/A)$, and $\hat{D} = D[\ln(1/A)]^2$, exhibiting the retention of dependence on A.

For bounded r, as in any computation, the tails of the PDF are truncated and the solution between the bounds deviates from log-normal form. For these reasons, computed PDFs $P(r)$ must be scaled by a time dependent normalization factor.

Lundgren (1981) likewise obtains log-normally distributed $P(r)$ for the viscous range, but his theory yields a different differential equation whose solution gives the result $\hat{V}/\hat{D} = 3$, while the HiPS value is $2/[3\ln(1/A)]$. The Lundgren value is matched for $A = \exp(-2/9) = 0.8$. The default value $A = 0.5$ corresponds to a value of $\hat{V}/\hat{D}$ that is lower than the Lundgren value, implying higher diffusive spreading of the PDF relative to its drift toward large scales.

In view of the demonstration in section 3.3.2 that A, evaluated as $2^{-1/3}$ but fortuitously within 1% of 0.8, is the physically most realistic value from a dimensional viewpoint, all available evidence indicates that $A = 0.8$ is the physically most justified choice.

The Lundgren (1981) viscous-range result holds for all spatial dimensions. This could be related to the lack of A dependence of P_k stemming from substitution of $B = 1$ into equation A 1, highlighting the distinction between the internal consistency of HiPS and the issues that arise when transforming to physical space.

Regarding the accuracy of the Taylor-series truncation in equation A 2, the discussion of figure 8 highlights the close agreement between the analytically derived PDF for the viscous range and the exact numerical result. A more definitive test is comparison of the equilibrium PDF shape obtained from the specialization of equation A 2 to stationarity and the exact equilibrium result, equation 3.3. (To verify that stationarity corresponds to equilibrium, note that the exact equilibrium result satisfies equation A 1 with the left-hand side set equal to zero.) For the viscous range, substitution of $B = 1$ and the *ansatz* $P_k \propto q^k$ into equation A 2 yields the stationary solution $q = \exp(2/3) = 1.95$, indicating

that, at least for this regime, the Taylor-series truncation is fairly accurate albeit inexact.

Relaxation of the restriction $B = 1$ yields a B-dependent stationary solution of equation A 2, with $q = 2$ only for an A value close to 0.6. For the A values of interest, the deviations from the exact stationary solution are not large, but this is ultimately immaterial. The only tangible present benefit of equation A 2 is that its specialization to equation A 5 transparently exhibits the dispersion phenomenology in a manner that led to the parameter assignment $A = 0.8$ and thus to predictive capability across scaling regimes.

It is instructive to compare the foregoing viscous-range results to LEM behavior in this regime. As in HiPS, advection is represented in LEM by instantaneous rearrangements of parcel locations, but in LEM they are applied along a one-dimensional domain. Each of these 'triplet maps' applies threefold compression to a chosen size-ℓ interval, fills the interval with three copies of this compressed image, and flips the middle image to maintain the spatial continuity of parcel property profiles. ℓ is assumed to be the same for all maps, where ℓ can be viewed as the smallest of a range of map sizes extending into the inertial range, or equivalently as representative of the full range of map sizes, because the results of interest are unaffected by the choice of interpretation.

As above, the initial condition $P(r, t = 0) = \delta(r - r_0)$ is assumed where $r_0 \ll \ell$. The latter condition assures that it is rare for only one of the two parcels to reside in a size-ℓ mapped interval. Then the leading-order case is that both parcels are mapped. Viewing the spatially continuous map as the continuum limit of spatially discrete maps (permutations) with successively greater spatial refinement, it has been shown (Fistler *et al.* 2020) that the mathematically consistent mapping procedure is to randomly and independently assign each of the parcels, now treated as marker points, to one of the three compressed images.

Accordingly, the markers are assigned to the same image with probability 1/3, in which case their separation is reduced by a factor of three. Otherwise their separation is typically increased to order ℓ, in which case their subsequent motions are deemed to be irrelevant to the scale-r_0 time advancement of $P(r, t)$. Then for order-r_0 pair separation, r is subject to successive three-fold reductions such that $r(t) = 3^{-n(t)} r_0$, where the statistics of the number $n(t)$ of map applications during $[0, t]$ determines $P(r, t)$ in $[0, r_0]$. The argument r is thus discretized into levels $3^{-n} r_0$ so $P(r)$ (suppressing t) is discretized as P_n, which obeys

$$\frac{dP_n}{dT} = \frac{1}{3} P_{n-1} - P_n. \tag{A 6}$$

Here, the rate of map occurrences is absorbed into the normalized time T and the coefficient 1/3 reflects the 2/3 probability that a map results in a pair separation beyond the range of interest. This causes a decrease in time of $\sum_{n=0}^{\infty} P(n)$, where this sum will be used to normalize $P(n)$ to unity within the range of interest.

The solution $P_n = 3^{-n} e^{-T}$ yields the time-invariant normalized form $P_n = 2 \cdot 3^{-n-1}$, corresponding to $P_r = (2r/3r_0)$ in terms of the discrete set of pair separations r. Converting to continuous r based on $dn/dr = -r_0/(r \ln 3)$ gives constant $P(r)$, which is the dimensionally correct equilibrium scaling for a one-dimensional domain but is not realizable in one dimension because it is not normalizable on an unbounded r interval.

Separation of variables does not yield a transient solution to the initial-value problem of interest. To formally exhibit the phenomenology, equation A 6 is

Taylor expanded to obtain

$$\frac{\partial P_n}{\partial T} = \frac{1}{6}\frac{\partial^2 P_n}{\partial n^2} - \frac{1}{3}\frac{\partial P_n}{\partial n} - \frac{2}{3}P_n. \tag{A 7}$$

The positive second derivative indicates diffusive spreading that reflects the ensemble statistics of mapping occurrences. The negative first derivative indicates drift toward larger n, hence smaller r, reflecting the monotonically decreasing separation of markers with initial separation $r_0 \ll \ell$. The rightmost term reflects strongly nonlocal jumps to r of order ℓ, here formalized as a loss term because these marker pairs are transferred away from the space-time regime relevant to time advancement initialized with separation r_0.

These considerations merely formalize the consequences of the anomaly that the effects of a triplet map at a much smaller scale than its size are qualitatively correct in that the map induces both compressive and extensive strain, but the extensive strain as embodied in the multiplicatively large increases of particle separation grossly exaggerates the scale-r_0 extensive-strain effect of a scale-ℓ eddy. Relative to LEM, HiPS is physically more accurate in this regard because the swap-induced multiplicative change of particle separation is of order unity regarless of whether the separation increases or decreases.

In other respects, such as mixing advancement based on fully resolved gradient-driven diffusive fluxes using the true molecular-transport coefficients, LEM is more accurate than HiPS. On balance, there is a trade-off between the two formulations, with the preference between them dependent on the specific needs of individual applications.

Appendix B. Analysis of mixing in a three-level tree

The HiPS flux, production, and dissipation are evaluated directly for a three-level tree. Refer to table A1. Let the four parcels have initial values $(0, 0)$, $(1, 1)$, where parentheses indicate half-trees, giving $\Delta\phi_0 = 1$. Only level-0 swaps are possible. With equal likelihood, a swap is either jump-periodic (JP), corresponding to flux between hypothetically adjacent domain boundaries, or internal (I), corresponding to flux across the domain center. As in the usual representation of an imposed mean scalar gradient, a JP swap enforces jump-periodicity by adding ± 2 to the scalar value of each parcel deemed to exit and re-enter the domain, where the direction of displacement determines the sign of this adjustment. We can ignore permutations within a half-tree without loss of generality.

This three-level model implementation has distinctive features that do not apply to cases with four or more levels. Each eddy event produces one of two distinct final system states: $(1/2, 1/2)$, $(1/2, 1/2)$, or $(-1/2, -1/2)$, $(3/2), 3/2)$, which are uniform and nonuniform, respectively. Starting from either of the two states, the system state is uniform after a type-I event, and nonuniform after a type-JP event. The half-tree mean values $\langle\phi\rangle$, and variances $\langle\phi'^2\rangle$ after each of swap and mixing operations comprising the eddy event are shown in the table. $\langle\phi'^2\rangle$ is computed as the mean square difference between the parcel values in the half-tree and the imposed ensemble mean value (0 or 1) in the half-tree. An eddy event preceded by an eddy event of the same type produces no state change. In effect, the system evolves only when two events of different type occur in

Table A1: HiPS state evolution for a three-level tree. Parentheses group parcel values in half-trees. EE refers to an eddy event involving a swap of type jump-periodic (JP) or internal (I) followed by mixing of parcel pairs. Subscripts on half-tree averages designate the different stages of evolution.

Initial state	(0,0), (1,1)						
$\langle\phi\rangle_0$	0 1						
$\langle\phi'^2\rangle_0$	0 0						

First EE: I or JP	I (applied to initial state)			JP (applied to initial state)			
After swap	(0, 1), (0, 1)			(-1, 0), (1, 2)			
After mixing	$(\frac{1}{2}, \frac{1}{2})$, $(\frac{1}{2}, \frac{1}{2})$			$(-\frac{1}{2}, -\frac{1}{2})$, $(\frac{3}{2}, \frac{3}{2})$			
$\langle\phi\rangle_1$	$\frac{1}{2}$ $\frac{1}{2}$			$-\frac{1}{2}$ $\frac{3}{2}$			
$\langle\phi'^2\rangle_1$	$\frac{1}{4}$ $\frac{1}{4}$			$\frac{1}{4}$ $\frac{1}{4}$			

Next EE: I or JP	JP	I	JP	I
After swap	$(-\frac{3}{2}, \frac{1}{2})$, $(\frac{1}{2}, \frac{5}{2})$	$(\frac{1}{2}, \frac{1}{2})$, $(\frac{1}{2}, \frac{1}{2})$	$(-\frac{1}{2}, -\frac{1}{2})$, $(\frac{3}{2}, \frac{3}{2})$	$(-\frac{1}{2}, \frac{3}{2})$, $(-\frac{1}{2}, \frac{3}{2})$
$\langle\phi\rangle_2$	$-\frac{1}{2}$ $\frac{3}{2}$	$\frac{1}{2}$ $\frac{1}{2}$	$-\frac{1}{2}$ $\frac{3}{2}$	$\frac{1}{2}$ $\frac{1}{2}$
$\langle\phi'^2\rangle_2$	$\frac{5}{4}$ $\frac{5}{4}$	$\frac{1}{4}$ $\frac{1}{4}$	$\frac{1}{4}$ $\frac{1}{4}$	$\frac{5}{4}$ $\frac{5}{4}$
After mixing	$(-\frac{1}{2}, -\frac{1}{2})$, $(\frac{3}{2}, \frac{3}{2})$	$(\frac{1}{2}, \frac{1}{2})$, $(\frac{1}{2}, \frac{1}{2})$	$(-\frac{1}{2}, -\frac{1}{2})$, $(\frac{3}{2}, \frac{3}{2})$	$(\frac{1}{2}, \frac{1}{2})$, $(\frac{1}{2}, \frac{1}{2})$
$\langle\phi\rangle_3$	$-\frac{1}{2}$ $\frac{3}{2}$	$\frac{1}{2}$ $\frac{1}{2}$	$-\frac{1}{2}$ $\frac{3}{2}$	$\frac{1}{2}$ $\frac{1}{2}$
$\langle\phi'^2\rangle_3$	$\frac{1}{4}$ $\frac{1}{4}$	$\frac{1}{4}$ $\frac{1}{4}$	$\frac{1}{4}$ $\frac{1}{4}$	$\frac{1}{4}$ $\frac{1}{4}$

	JP	I	JP	I
$\langle\phi\rangle_3 - \langle\phi\rangle_1$	-1 1	0 0	0 0	1 -1
$\langle\phi'^2\rangle_2 - \langle\phi'^2\rangle_1$	1 1	0 0	0 0	1 1
$\langle\phi'^2\rangle_3 - \langle\phi'^2\rangle_2$	-1 -1	0 0	0 0	-1 -1

Repeat, I or JP EE	. . .						

succession, so the evolution consists of back-and-forth switches from one state to the other.

Consider the flux through the domain center, arising from internal swaps. These result in $\langle\phi\rangle_3 - \langle\phi\rangle_1$ equal to 0 or -1 in the right half-tree, and 0 or 1 in the left half-tree. The average time between internal swaps is $2\tau_0$, so the average $d(\langle\phi\rangle_3 - \langle\phi\rangle_1)/dt$ in the right half-tree is $-1/(4\tau_0)$. Using this in equation 3.11 recovers the nondomensional flux of $-1/8$, equation 3.10.

The production $\mathcal{P}$ is the average rate of change of variance due to swaps,

which happen at mean rate $1/\tau_0$. This production is given by the mean (over the four columns of table A1) of $(\langle\phi'^2\rangle_2 - \langle\phi'^2\rangle_1)/\tau_0 = 1/(2\tau_0)$, which recovers the nondimensional production of $1/2$, equation 3.13.

Similarly, the mean dissipation rate $\langle\chi\rangle$ is the negative of the average rate of change of variance due to mixing occurrences, which happen at mean rate $1/\tau_0$. This dissipation is given by the mean (over the four columns of table A1) of $-(\langle\phi'^2\rangle_3 - \langle\phi'^2\rangle_2)/\tau_0 = 1/(2\tau_0)$, which recovers the nondimensional dissipation value $1/2$, equation 3.14.

REFERENCES

ARGYROPOULOS, C. D. & MARKATOS, N.C. 2015 Recent advances on the numerical modelling of turbulent flows. *Applied Mathematical Modelling* **39**, 693–732.

BATCHELOR, G. K. 1959 Small-scale variation of convected quantities like temperature in a turbulent fluid. Part 1. General discussion and the case of small conductivity. *Journal of Fluid Mechanics* **5**, 113–133.

CABRA, R., CHEN, J.Y., DIBBLE, R.W., KARPETIS, A.N. & BARLOW, R.S. 2005 Lifted methane–air jet flames in a vitiated coflow. *Combustion and Flame* **143** (4), 491–506.

CABRA, R., MYHRVOLD, T., CHEN, J.Y., DIBBLE, R.W., KARPETIS, A.N. & BARLOW, R.S. 2002 Simultaneous laser Raman-Rayleigh-LIF measurements and numerical modeling results of a lifted turbulent H_2/N_2 jet flame in a vitiated coflow. *Proceedings of the Combustion Institute* **29** (2), 1881–1888.

CHEN, C., GAO, T., LIANG, J., ZHANG, L. & SUN, M. 2024 Advances and challenges in developing a stochastic model for multi-scale fluid dynamic simulation: One-dimensional turbulence. *Chinese Journal of Aeronautics* **in press**.

CHERTKOV, M., FALKOVICH, G. & KOLOKOLOV, I. 1998 Intermittent dissipation of a passive scalar in turbulence. *Physical Review Letters* **80**, 2121–2124.

CHURCHILL, S.W. 2002 A reinterpretation of the turbulent Prandtl number. *Industrial and Engineering Chemistry Research* **41**, 6393–6401.

CRAWFORD, F. W., HO, L. S. T. & SUCHARD, M. A. 2018 Computational methods for birth-death processes. *Wiley Interdisciplinary Reviews: Computational Statistics* **10**, e1423.

CURL, R. L. 1963 Dispersed phase mixing: I. Theory and effects in simple reactors. *AIChE Journal* **9**, 175–181.

DONZIS, D. A., SREENIVASAN, K. R. & YEUNG, P. K. 2010 The Batchelor spectrum for mixing of passive scalars in isotropic turbulence. *Flow, Turbulence and Combustion* **85**, 549–566.

ECHEKKI, T. 2008 Stochastic modeling of autoignition in turbulent non-homogeneous hydrogen-air mixtures. *International Journal of Hydrogen Energy* **33**, 2596–2603.

ELSINGA, G., ISHIHARA, T. & HUNT, J. 2022 Non-local dispersion and the reassessment of Richardson's t^3-scaling law. *Journal of Fluid Mechanics* **932**, A17.

FISTLER, M., KERSTEIN, A.R., WUNSCH, S. & OEVERMANN, M. 2020 Turbulence modulation in particle-laden stationary homogeneous shear turbulence using one-dimensional turbulence. *Physical Review Fluids* **5**, 124303.

FOX, RODNEY O. 2003 *Computational models for turbulent reacting flows*. Cambridge University Press.

GOSHAYESHI, B & SUTHERLAND, J.C. 2015 Prediction of oxy-coal flame stand-off using high-fidelity thermochemical models and the one-dimensional turbulence model. *Proceedings of the Combustion Institute* **35**, 2829–2837.

GOTOH, T. & WATANABE, T. 2015 Power and nonpower laws of passive scalar moments convected by isotropic turbulence. *Physical Review Letters* **115**, 114502.

GURVICH, A. S. & YAGLOM, A. M. 1967 Breakdown of eddies and probability distributions for small-scale turbulence. *Physics of Fluids* **10**, 59–65.

HEWSON, J. C. & KERSTEIN, A. R. 2001 Stochastic simulation of transport and chemical kinetics in turbulent $CO/H_2/N_2$ flames. *Combustion Theory and Modelling* **5**, 669–697.

HOLTZER, M. & SIGGIA, E.D. 1994 Turbulent mixing of a passive scalar. *Physics of Fluids* **6**, 1820–1837.

JULLIEN, M., PARET, J. & TABELING, P. 1998 Richardson pair dispersion in two-dimensional turbulence. *Physical Review Letters* **82**, 2872–2875.

KALDA, J. & MOROZENKO, A. 2008 Turbulent mixing: the roots of intermittency. *New Journal of Physics* **10**, 093003.

KERSTEIN, A. R. 1991 Linear-eddy modelling of turbulent transport. Part 6. Microstructure of diffusive scalar mixing fields. *Journal of Fluid Mechanics* **231**, 361–394.

KERSTEIN, A. R. 2013 Hierarchical parcel-swapping representation of turbulent mixing. Part 1. Formulation and scaling properties. *Journal of Statistical Physics* **153**, 142–161.

KERSTEIN, A. R. 2014 Hierarchical parcel-swapping representation of turbulent mixing. Part 2. Application to channel flow. *Journal of Fluid Mechanics* **750**, 421–463.

KERSTEIN, A. R. 2021 Hierarchical parcel-swapping representation of turbulent mixing. Part 3. Origins of correlation patterns observed in turbulent boundary layers. *Physical Review Fluids* **6**, 044611.

KERSTEIN, A. R. 2022 Reduced numerical modeling of turbulent flow with fully resolved time advancement. Part 1. Theory and physical interpretation. *Fluids* **7**, 76.

KESSOURI, F., ULSES, C., ESTOURNEL, C., MARSALEIX, P., D'ORTENZIO, F., SEVERIN, T., TAILLANDIER, V. & CONAN, P. 2018 Vertical mixing effects on phytoplankton dynamics and organic carbon export in the western mediterranean sea. *Journal of Geophysical Research: Oceans* **123** (3), 1647–1669.

KLEIN, M., ZENKER, C., STARICK, T. & SCHMIDT, H. 2023 Stochastic modeling of multiple scalar mixing in a three-stream concentric coaxial jet based on one-dimensional turbulence. *International Journal of Heat and Fluid Flow* **104**, 109235.

KOLMOGOROV, A. N. 1962 A refinement of previous hypotheses concerning the local structure of turbulence in a viscous in-compressible fluid at high Reynolds number. *Journal of Fluid Mechanics* **13**, 82–85.

KRAICHNAN, R.H. 1968 Small-scale structure of a scalar field convected by turbulence. *Physics of Fluids* **11**, 945–953.

KRAICHNAN, R.H. 1974 Convection of a passive scalar by a quasi-uniform random straining field. *Journal of Fluid Mechanics* **64**, 737–762.

LI, D. 2019 Turbulent Prandtl number in the atmospheric boundary layer–where are we now? *Atmospheric Research* **216**, 86–105.

LIGNELL, D. O., FREDLINE, G. C. & LEWIS, A. D. 2015 Comparison of one-dimensional turbulence and direct numerical simulations of soot formation and transport in a nonpremixed ethylene jet flame. *Proceedings of the Combustion Institute* **35**, 1199–1206.

LIM, H. D., GRYLLS, T., GOUGH, H., REEUWIJK, M., GRIMMOND, S. & VANDERWEL, C. 2022 Pollutant dispersion by tall buildings: laboratory experiments and large-eddy simulation. *Experiments in Fluids* **63** (92), 1–20.

LUNDGREN, T.S. 1981 Turbulent pair dispersion and scalar diffusion. *Journal of Fluid Mechanics* **111**, 27–57.

OBUKHOV, A. M. 1941 Spectral energy distribution in turbulent flow. *Izvestiya Akademii Nauk:SSSR. Seriya Matematicheskaya* **5**, 453–566.

OBUKHOV, A. M. 1962 Some specific features of atmospheric turbulence. *Journal of Fluid Mechanics* **13**, 77–81.

OEVERMANN, M., SCHMIDT, H. & KERSTEIN, A. R. 2008 Investigation of autoignition under thermal stratification using linear eddy modeling. *Combustion and Flame* **155**, 370–379.

POPE, S. B. 2000 *Turbulent flows*. New York: Cambridge University Press.

RICHARDSON, L. 1926 Atmospheric diffusion shown on a distance-neighbour graph. *Proceedings of the Royal Society of London Series A, Containing Papers of a Mathematical and Physical Character,* **110**, 709–737.

SAWFORD, B.L. 2001 Turbulent relative dispersion. *Annual Review of Fluid Mechanics* **33**, 289–317.

SAWFORD, B.L. & PINTON, J.F. 2013 A Lagrangian view of turbulent dispersion and mixing. In *Ten Chapters in Turbulence* (ed. P.A. Davidson, Y. Kaneda & K. Sreenivasan), pp. 132–175. Cambridge.

SCATAMACCHIA, R., BIFERALE, L. & TOSCHI, F. 2012 Extreme events in the dispersion of two neighboring particles under the influence of fluid turbulence. *Physical Review Letters* **45**, 14501.

SHRAIMAN, B.I. & SIGGIA, E.D. 1994 Lagrangian path integrals and fluctuations in random flow. *Physical Review E* **49**, 2912–2927.

SREENIVASAN, K. R. 2019 Turbulent mixing: a perspective. *Proceedings of the National Academy of Sciences* **116**, 18175–18183.

SU, L. K. & CLEMENS, N. T. 2003 The structure of fine-scale scalar mixing in gas-phase planar turbulent jets. *Journal of Fluid Mechanics* **488**, 1–29.

SUBRAMANIAM, S. & POPE, S. B. 1998 A mixing model for turbulent reactive flows based on euclidean minimum spanning trees. *Combustion and Flame* **115**, 487–514.

YEUNG, P. K. & SREENIVASAN, K. R. 2013 Spectrum of passive scalars of high molecular diffusivity in turbulent mixing. *Journal of Fluid Mechanics* **716**, R14.

YEUNG, P. K. & SREENIVASAN, K. R. 2014 Direct numerical simulation of turbulent mixing at very low Schmidt number with a uniform mean gradient. *Physics of Fluids* **26** (1).

ZHAO, Y. 2021 Turbulence theories and statistical closure approaches. *Physics Reports* **935**, 1–117.

ZIMBERG, M. J., FRANKEL, S. H., GORE, J. P. & SIVATHANU, Y. R. 1998 A study of coupled turbulent mixing, soot chemistry, and radiation effects using the linear eddy model. *Combustion and Flame* **113**, 454–469.